Taylor bubble formation and flowing in a straight millimetric channel with a cross-junction inlet geometry Part I: Bubble dynamics

Mei Mei, Claude Le Men, Karine Loubière, Gilles Hébrard, N. Dietrich

Highlights

- Taylor bubble formation dynamics were studied at a cross-junction.
- Filling and squeezing stage frequencies were not controlled by the same parameters.
- Gas finger lengths were measured to identify different bubble pinch-off patterns.
- A simple relationship linking relative bubble lengths with j_{G0}/j_{L} was established.

Taylor bubble formation and flowing in a straight millimetric channel with a cross-junction inlet geometry

Part I: Bubble dynamics

Mei Mei[1,2,3], Claude Le Men[1,3], Karine Loubière[2,3], Gilles Hébrard[1,3],

Nicolas Dietrich[1*,3]

[1] Toulouse Biotechnology Institute, Université de Toulouse, CNRS, INRAE, INSA, Toulouse, France

[2] Laboratoire de Génie Chimique, Université de Toulouse, CNRS, INP, UPS, Toulouse, France

[3] Fédération de Recherche FERMAT, CNRS, Toulouse, France

*Corresponding author: Dr. Nicolas Dietrich

E-mail: nicolas.dietrich@insa-toulouse.fr

Abstract

The investigations of bubble formation dynamics at a cross-junction in a straight milli-channel were reported. The bubble formation process could be divided into the filling and squeezing stages, and their frequencies were compared at various conditions. It was found that the filling and squeezing frequencies were controlled mainly by the gas and liquid superficial velocities, respectively. The bubble formation frequencies could be related to the gas-liquid superficial velocity ratios, the liquid superficial velocities, and the bubble length. The bubble formation process was then analyzed considering the length of the gas finger right after the bubble pinch-off. Two patterns were identified depending on whether the pinch-off occurred inside of the cross-junction or not. The transition between these two patterns was described by a critical liquid Capillary number. Furthermore, the squeezing and dripping patterns were distinguished as the gas finger could fully block the channel or not. The transitions between the bubble formation patterns were determined by the gas Weber number and liquid Capillary number. Finally, the bubble length, the liquid slug length, and the bubble length normalized by the unit cell length could all be predicted based on the gas-liquid superficial velocity ratios η_0.

Keywords: Taylor flow. Bubble formation. Cross-junction. Bubble pinch-off. Pattern transition.

1. Introduction

The microtechnology devices to put gas and liquid in contact allow producing highly regular, repeatable, and mono-dispersed bubbles and liquid slugs, which could be found in numerous applications of chemical, biology, and pharmaceutical engineering (Geng et al., 2020; Xu et al., 2021), and in many other fields. In the meantime, multiphase reactions, mixing, or separations are usually involved. Each liquid slug could be considered as an individual microfluidic reactor that is isolated from each other by the bubbles. For that, special attention should be paid to the bubble formation process, which has been extensively investigated through experimental and simulation methods (Yao et al., 2021), because the question of "when and how bubble pinch-off happens" directly determines the bubble and liquid slug size, frequency and flow regimes (Dang et al., 2013; Haase, 2017).

The main factors influencing the bubble pinch-off in microfluidic devices were found as follows: the confinement space or channel geometry (Garstecki et al., 2006; Dietrich et al., 2008), the gas-liquid superficial velocity ratio (Garstecki et al., 2006), the rheology of the liquid phase (Lu et al., 2014a; Zhang et al., 2017; Sontti et al., 2019), the surface tension (Shao et al., 2008; Lu et al., 2014b; Li et al., 2021), the presence of surfactants (Li et al., 2020). In particular, the channel geometry could be further identified by the inlet geometry (e.g., T-junction, flow-focusing/cross-junction, and co-flowing geometries), wettability of channel, and cross-sectional shapes (Garstecki et al., 2006). Despite the regularity of the bubble and liquid slugs, a universal predictive model without empirical coefficients is still in demand to get a thorough understanding of the bubble formation dynamics and size predictions (Svetlov and Abiev, 2021).

The bubble formation mechanisms in microfluidic devices were commonly classified into three patterns (Fu and Ma, 2015; Yao et al., 2021), i.e., squeezing, dripping (shearing), and jetting regimes, which were generally

analyzed through image analysis from experimental data, theoretical modeling, or numerical simulations. Recently, Korczyk et al. (2019) revealed an additional leaking regime accounting for the corner flow, which clarified the lowest boundaries for squeezing regimes at low capillary numbers. The bubble breakup patterns were influenced by the balance between the forces acting on the gas finger (or gas thread), namely interfacial force, viscous shear force, pressure gradient along the bubble and inertia force (Dollet et al., 2008).

Among them, the jetting regime (Xu et al., 2014) was usually encountered under high capillary numbers. The bubbles were pinched-off by the surrounding liquid downstream of the inlet (e.g., cross-junction, or gas micro-capillary). The pinch-off was thus triggered by the balance between viscous shear force and interfacial force (Fu et al., 2009; Castro-Hernández et al., 2011). In the jetting regime, the generated bubble sizes were far smaller compared to the channel size. The dripping (shearing) regime (De Menech et al., 2008) was a transition regime between the squeezing and jetting regimes, which was also encountered under high Capillary number. The gas phase entered the main channel without blocking it, making possible for the liquid phase to freely bypass the gas thread. The viscous shear force also took a major role in rupturing bubbles, which were detached near the cross junction or gas micro-capillary. For the squeezing regime (Garstecki et al., 2006), the dispersed phase penetrated into the main channel, propagated towards the wall and downstream, resulting in a blockage of the continuous phase flow. Due to this blockage, the increased pressure force induced at the upstream of the gas thread finally triggered the breakup. The interfacial force dominated the viscous force (i.e., low Capillary numbers). Furthermore, the generated bubble and droplet lengths in the squeezing regime were almost independent on the capillary numbers, unlike the other regimes.

Concerning the transitions between these formation regimes, Garstecki et al. (2006) found that the transition between the squeezing and dripping regimes occurred at a critical Capillary number equal to 10^{-2}. Later Xu et al. (2008) and

Fu et al. (2010b) further specified the Capillary number ranges for different formation regimes: for squeezing and shearing regimes, they were identified from 10^{-4} to 0.0058 and from 0.013 to 0.1, respectively. In addition, at a medium range of Ca (0.0058-0.013), both squeezing pressure and the shearing force affected the collapse. This transition regime was defined as 'squeezing to dripping' regime (Xu et al., 2008; Fu et al., 2011).

However, some researchers found that it is difficult to determine the transition boundaries simply basing on the Capillary numbers. Recently, Sontti and Atta (2019) identified the droplet formation maps depending on the continuous phase (i.e., water) Capillary number and the dispersed phase (i.e., oil) Weber number, and they demonstrated the transition boundaries between different regimes. This work also highlighted the critical role of dispersed Weber numbers. Furthermore, Madana and Ali (2020) simulated the droplet formation using VOF method in a T-junction and classified the droplet formation regimes to five types. This flow regime map indicated that the droplet formation regimes and their transitions were governed by two-phase Capillary numbers and gas-liquid flow rate ratio. However, the transition boundaries between different formation regimes were generally plotted by the regime maps (Liu and Zhang, 2011; Li et al., 2019) and not quantitatively characterized. Accounting for the corner flow, Korczyk et al. (2019) investigated the droplet formation in a square T-junction and identified the lower and upper bounds of the squeezing regime, corresponding to the transitions to the leaking and jetting regimes. The transitions could be described in terms of the normalized droplet size as a function of the continuous phase Capillary number and the ratio between the dispersed and continuous phase flow rates (Schuler et al., 2021).

Concerning the bubble formation process, three stages could be identified (Abadie, 2013): filling (or expansion) (Fu et al., 2009), squeezing (or collapse) (Fu et al., 2010a), and fast pinch-off (or nonlinear breakup) (Lu et al., 2014b). Garstecki et al. (2005) were the pioneers to explore the squeezing stage and bubble

breakup in confined channels. They analyzed the thinning rate of the minimum width of the gas thread and found that it could be described by a linear collapse and a non-linear breakup, which was determined by the confinement of the channel and the Rayleigh-Plateau instability, respectively. Later on, many researchers (Garstecki et al., 2006; Dollet et al., 2008; Fu et al., 2010a; Lu et al., 2014b) further investigated the minimum width of the gas finger w_{neck} and found a power law relationship with the remaining time t_{remain} until pinch-off. The power law exponent ϑ was found at 1/3 (Dollet et al., 2008; Fu et al., 2010a) or 2/5 (Van Hoeve et al., 2011) or 1/2 (Lu et al., 2014b) or 1/6 for non-Newtonian liquid (Fu et al., 2012). Apart from the width of the gas thread, Li et al. (2020) showed that the pinch-off positions may change slightly at different breakup loops. Therefore, further studies about the axial position of gas finger right after the bubble pinch-off (or the axial position of minimum gas thread neck right before breakup) need to be implemented to give more accurate quantitative descriptions between different formation regimes.

The Part I of the present work aims at filling this research gap by proposing deeper investigations on the Taylor bubble formation process at a cross-junction inlet geometry. It will also serve as a basis for analyzing the gas-liquid mass transfer occurring during this bubble formation process (Part II). The present paper is structured as following. Section 2 will describe the experimental setup, image post-treatments and data processing implemented for studying bubble formation dynamics. In sub-sections 3.1 and 3.2, the bubble formation mechanism will be presented in terms of characteristic frequency and pattern, while the sub-section 3.3 will focus on the flow regimes and bubble shapes. In the sub-sections 3.4, the bubble lengths, liquid slug length and bubble velocities will be discussed according to the gas-liquid superficial velocity ratio and two-phase superficial velocities.

2. Materials and methods

2.1 Experimental setup

The experimental setup is illustrated in Fig. 1. The device was fabricated in a transparent polymethylmethacrylate (PMMA) plate (100×600×2 mm^3) and sandwiched by other two PMMA plates (100×600×4 mm^3) with screws and sealing rings. The contacting geometry to generate bubbles is a cross-junction, in which the two fluids merged in a cross where the gas was flowing in the main channel and the liquid was supplied with two orthogonal channels to squeeze the bubbles. All the channels, including the injection inlets of gas and liquid, and the main channel, were designed with the same square cross sections ($w^2 \cong 2\times2$ mm^2). The dimensions of the square channel deviated from 2 mm due to the manufacturing precision and mounting deformation of the channel. For this reason, the exact dimensions of the main channel will be calibrated firstly (see Supplementary Material S1, w_h = 2.19 mm, w_v= 2.13 mm, and w_{side}= 2.17 mm). The hydraulic diameter of the channel, noted d_h, were found equal to 2.16 ± 0.03 mm. The lengths of the gas inlet, liquid inlet and main channels were 30 mm, 45 mm, and 550 mm, respectively.

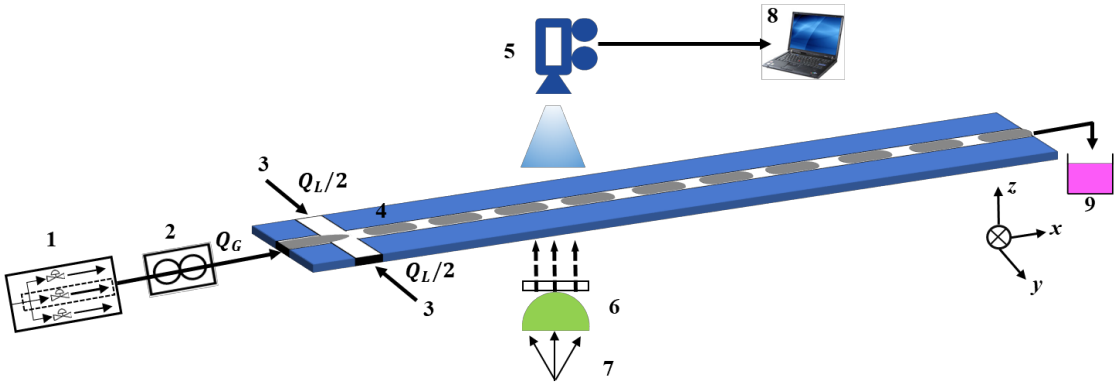

Fig. 1 Schematic representations of the experimental setup: 1. Lab air supply system, 2. Mass flow controller, 3. Liquid syringe pump, 4. Cross-junction straight milli-channel, 5. Camera, 6. Filter & Lens, 7. Green LED, 8. PC, 9. Collection beaker.

2.2 Flow control equipment

Air, as gas phase, was fed from house compressed air lines and the flow rate was controlled by a DPC17S-V0L6-BB5 airflow controller (calibrated under 101.4 kPa and 21.1 °C). Liquid solutions were both supplied from a 60 mL syringe in a syringe pump (Harvard Apparatus, PHD 22/2000, USA). The gas was introduced to the main channel and the liquid was injected perpendicularly from two side channels at the same flow rates ($Q_L/2$). After changing to a new flow rate condition, at least two times of residence time were considered to reach a steady gas-liquid flow. The gas superficial velocity j_{G0} ($j_{G0} = Q_{G0} / \Omega$), and liquid superficial velocity, j_L ($j_L = Q_L / \Omega$), were calculated by the associated volumetric flow rates (i.e., Q_{G0} and Q_L) and the cross-sectional area ($\Omega = {d_h}^2$). Due to the gas compressibility, the subscript 0 was added to explicitly indicate that the gas superficial velocity was calculated at the inlet position (j_{G0}). No equivalent subscript was used for the liquid phase as the liquid superficial velocity does not change along the channel's length. The gas superficial velocities j_{G0} ranged from 3.6 to 35.7 cm· s^{-1} and the liquid superficial velocities j_L ranged from 3.6 to 42.9 cm· s^{-1}. The total superficial velocity for two-phase flow j_{TP} ($j_{TP} = j_{G0} + j_L$) was defined as the summation of gas and liquid superficial velocities at the inlet. Correspondingly, the two-phase Capillary number Ca_{TP} ($Ca_{TP} = \frac{\mu_L j_{TP}}{\sigma_L}$) and Weber number We_{TP} ($We_{TP} = \frac{\rho_L {j_{TP}}^2 d_h}{\sigma_L}$) ranged from 1.6×10^{-3} to 8.5×10^{-3} and from 0.3 to 9.5, respectively.

2.3 Fluid properties

For investigating the bubble formation dynamics, the same liquid phase as the one used for gas-liquid mass transfer studies (Part II) was considered. It was composed of D-glucose anhydrous (Sigma Aldrich, CAS 50-99-7, noted GL) at a concentration of 20 $g \cdot L^{-1}$, sodium hydroxide (Sigma Aldrich, CAS 1310-73-2) at a concentration of 20 $g \cdot L^{-1}$, and resazurin (Sigma Aldrich, CAS 199303, purity 93%, noted RZ) at a concentration of 0.074 $g \cdot L^{-1}$ (corresponding to a maximal consumption concentration of oxygen, equal to 5.2 $mg \cdot L^{-1}$, see Part II). The physical-chemical properties of the liquid phase were measured by Dietrich et al. (2013). The liquid density, viscosity and surface tension are 1004.5 kg m^{-3}, 1.118 mPa s, and 75 mN m^{-1}, respectively. All experiments were conducted under atmospheric pressure (no counter-pressure valve was used at the outlet of the channel) and at room temperature (around 20° C).

2.4 Image acquisition and image processing

The gas-liquid flows were lighted by a M530L4 LED (Light-emitting diode, bandwidth at 35 nm) and images were recorded by a Basler acA1920-155µm camera (1920×1200 pixels, 12 bits) equipped with a 50 mm 1:1.4 Nikkor lens. This 530 nm wavelength of green LED was chosen in accordance with the absorption spectra of resorufin, which presented high absorbance near 530nm (see Supplementary Material S1). The LED was equipped to an aspheric condenser lens (ACL5040U-A, ϕ 50 mm) to generate parallel light beam and a NE2R10A absorptive ND filter was added to increase the LED intensity stability. The camera was set to work at a recording rate of 400 fps (i.e., acquisition time at 2.5 ms) with an exposure time of 22 µs. The spatial resolution of the images was at 8.25 µm per pixel. For all observing positions along the channel, a unique size of the region-of-interest (ROI) window was used: 1900×305 pixels (15.7×2.5 mm^2). Different ROI positions were shown in Supplementary Material S2.

By applying the procedures of image processing described in Mei et al. (2020) for raw images (Fig. 2 (a)), the bubbles and liquid slugs could be detected using the multilevel threshold based on Otsu's method (Otsu, 1979), shown in Fig. 2 (b) and (c), respectively. The hydrodynamic characteristics, such as the bubble length (L_B), velocity (U_B) and frequency (f_B), and the liquid slug length (L_S) (defined in Fig. 2), were also obtained by the original code in Matlab® R2017b.

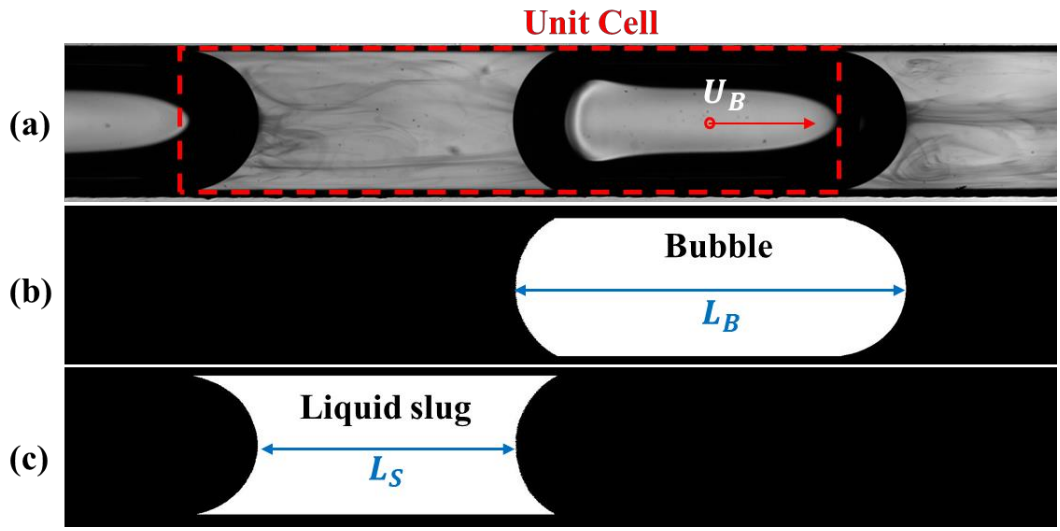

Fig. 2. Sequences of image processing implemented: (a) raw image, (b) detection of the bubble, (c) detection of the liquid slug. Operating condition: j_{G0} = 14.3 cm· s^{-1} and j_L = 14.3 cm· s^{-1}.

3. Results and discussion

3.1 Bubble formation dynamics

As discussed later (Fig. 5), the squeezing regime is dominant in the present work. Fig. 3 shows that, in this regime, three stages could be identified as below:

- Filling (also called expansion) stage, shown from Fig. 3 (c) to (h). The gas finger (defined as the coming gas thread) grew and entered the main channel until it occupied most of the channel. In the meantime, the liquid from two side channels passed around the gas finger.

– Squeezing (also called expansion) stage, shown from Fig. 3 (i) to (o). The channel was mainly blocked by the growing gas finger, and then the bubble neck was squeezed until reaching a minimum neck width.
– Fast pinch-off stage, shown from Fig. 3 (o) to (p). This stage could be considered as an instantaneous breakup. The characteristic time of this process was far smaller compared to the previous two stages. The bubble right after the pinch-off (indicated in the red dotted box) was elongated and would shrink under the interfacial tension force.

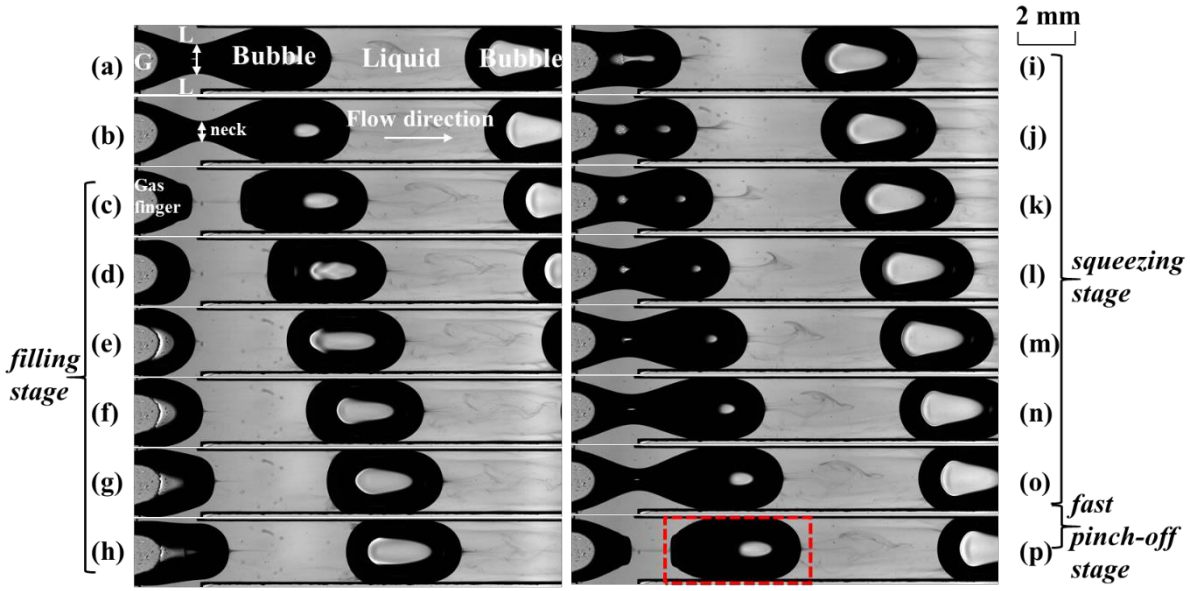

Fig. 3 Typical bubble formation process observed at the cross-junction. Operating conditions: j_L = 17.9 and j_{G0} = 10.7 cm· s^{-1}. The time interval between two images is 2.5 ms.

With the present image acquisition frequency (400 fps), the fast pinch-off stage was too fast to be accurately separated from the squeezing stage, and thus was included into the squeezing stage. Therefore, the overall bubble formation time, t_{BF}, could be defined as below:

$$t_{BF} = t_{filling} + t_{squeezing} \quad (1)$$

Considering the frequency of each stage, they could be presented as below:

$$\frac{1}{f_{BF}} = \frac{1}{f_{filling}} + \frac{1}{f_{squeezing}} \quad (2)$$

Fig. 4 (a) shows that the overall bubble formation frequencies f_{BF}, increased with the gas-liquid superficial velocity ratio η_0 ($\eta_0 = j_{G0} / j_L$) at a given j_L, and vice versa. Note that, for each operating condition, 500-1000 images were used to calculate the f_{BF}.

The bubble formation frequency could also be estimated from the gas volumetric flow rates Q_{G0} and the bubble volume V_B as:

$$f_{BF} = \frac{Q_{G0}}{V_B} = \frac{j_{G0}\,\Omega}{\varpi\, L_B\, \Omega} = \frac{\eta_0 j_L}{\varpi\, L_B} \quad (3)$$

where Ω is the cross-sectional area of the channel and ϖ represents the ratio between the bubble volume and the channel volume occupied with the same length of the bubble (accounting for the 3D bubble shape and the liquid films at walls around the bubble). Therefore, it was logical to observe that the bubble frequencies plotted in Fig. 4 increased with the liquid flow rates j_L and gas-liquid superficial velocity ratio η_0.

In addition, Fig. 4 (b) presents the variations of bubble formation frequencies during the filling stage and the squeezing stage versus η_0. It can be observed that the filling frequencies (represented by solid symbols) were mainly determined by the ratios η_0 and almost independent on the superficial liquid velocities j_L while the squeezing frequencies were controlled by both ratios η_0 and j_L. At a given j_L, these two frequencies increased with the ratio η_0. The operating conditions were chosen to cover significant ranges in terms of liquid and gas superficial velocities, and also the two-phase superficial velocities (j_{TP}) and gas-liquid superficial velocities ratios (η_0).

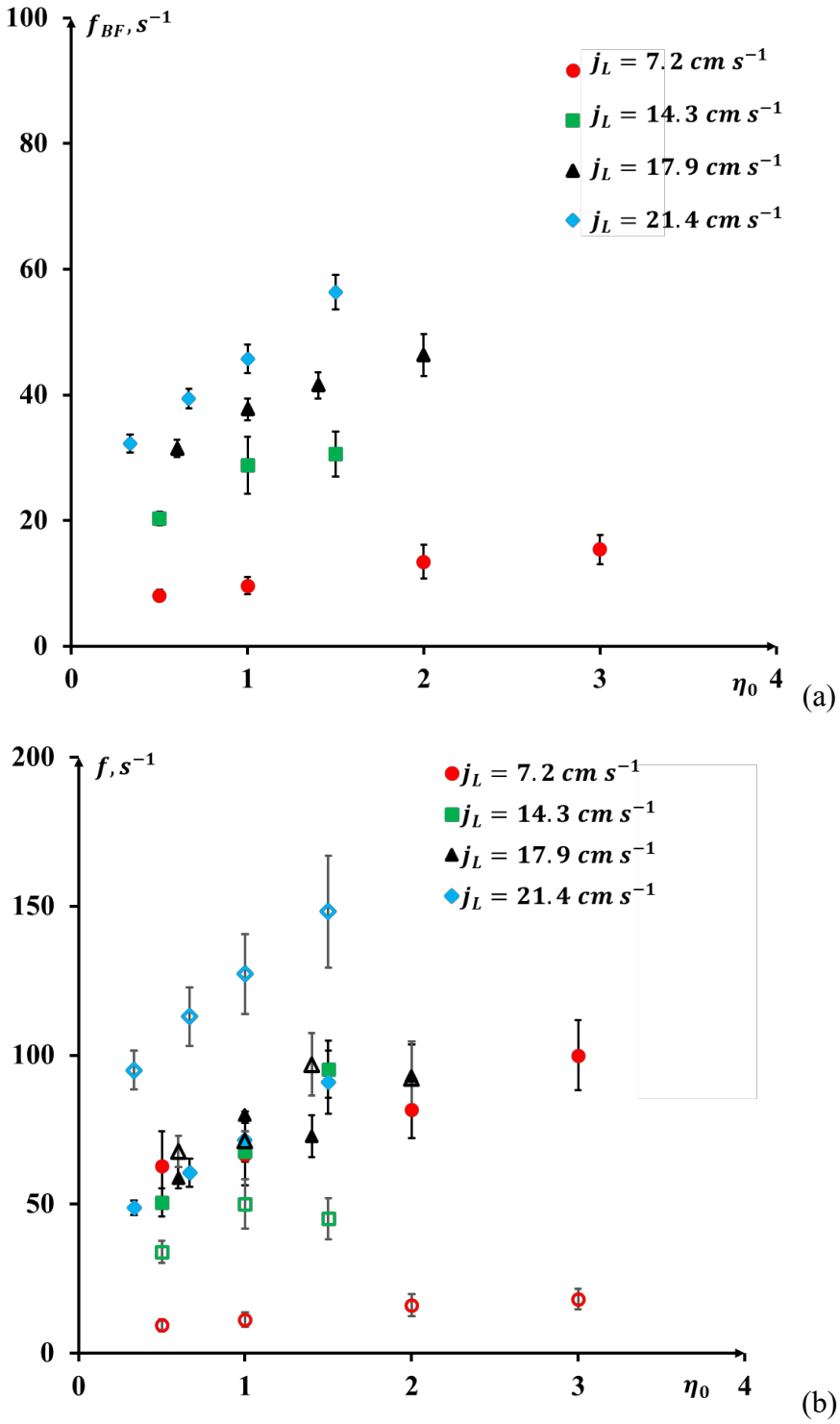

Fig. 4 Bubble formation: (a) overall frequencies, (b) frequencies for the filling stage (solid symbols) and for the squeezing stage (empty symbols), as a function of the gas-liquid superficial velocity ratio η_0.

When the bubble formation frequencies (overall, filling or squeezing frequencies) increased (and thus tended towards the image acquisition frequency),

the deviations induced by the image acquisition frequency (400fps) were inevitably higher, which could be seen from Fig. 4 (b) when the squeezing frequencies is higher than 100 Hz. In the future, a more advanced camera (with increased image acquisition frequency while conserving enough spatial resolution) should be used to obtain more accurate values for the overall bubble formation, filling and squeezing frequencies. All the frequencies plotted in Fig. 4 could be found in the Table S3 of the Supplementary Material S3.

3.2 Bubble formation patterns

Depending on the bubble shapes during and after the bubble formation, three bubble formation regimes are reported in the literature, i.e., squeezing, dripping, and jetting regimes. Fig. 5 displays typical instantaneous gas-liquid Taylor flows right after the bubble pinch-off for various operating conditions. The generated bubble lengths were always bigger than the channel width whatever the operating conditions. Referring to the classical description adopted for these regimes (i.e., whether the bubble totally blocked the channel or not), a deep analysis of the images reported in Fig. 5 showed that, in the present study, only the squeezing (e.g., a majority cases shown in Fig. 5) and dripping regimes (e.g., the case $Ca_{TP} = 8.5\times10^{-3}$, $j_L = 42.9$ cm s^{-1}, $j_{G0} = 14.3$ cm s^{-1}) took place.

Furthermore, one could observe that the gas finger lengths (i.e., the coming gas thread) right after the bubble pinch-off changed with the gas and liquid superficial velocities. Considering this parameter, two pinch-off patterns were identified:

- The pinch-off pattern type I, where the pinch-off of the bubble was located inside the cross-junction (i.e., without entering the main channel). This pattern was marked inside the dotted blue box in Fig. 5.
- The pinch-off pattern type II, where the pinch-off of the bubble was located outside the cross-junction (namely occurred inside the main

channel). This pattern was marked outside the dotted blue box in Fig. 5.

As observed in Fig. 5, at a given liquid superficial velocity, the pinch-off position was likely moving towards the main channel with the increase of gas superficial velocity (i.e., the transition from type I to type II), whereas the opposite trend was observed at a given gas superficial velocity and for increasing liquid superficial velocity. To quantify these observations, the gas finger length (noted l_{GF}) that was ruptured by the liquid right after the bubble pinch-off was measured by image processing, as illustrated in Fig. S 6 (Supplementary Material). By plotting this normalized gas finger length as a function of the gas-liquid superficial velocity ratio (see Fig. S 7 in the Supplementary Material), the two pinch-off patterns could be simply distinguished, depending on whether l_{GF}/w_{side} was higher or lower than one unit.

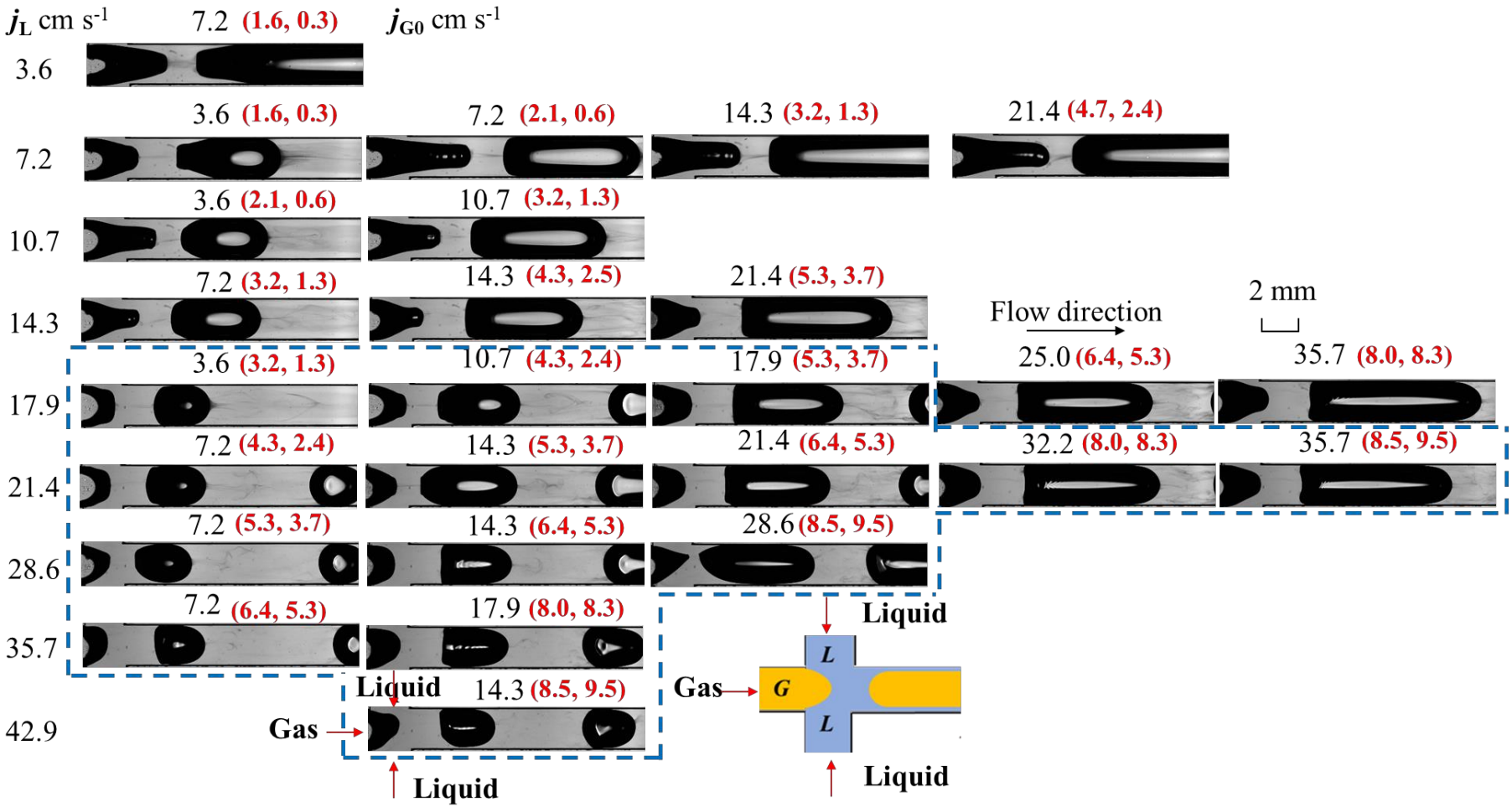

Fig. 5 Cartography of gas-liquid Taylor flows right after the bubble pinch-off at the cross- junction position ($X_1 = 0$), for various operating conditions. The dimensionless numbers in the red brackets correspond to ($Ca_{TP}\times10^{-3}$, We_{TP}). The pinch-off patterns of type I and II are located inside and outside of the dotted blue box respectively.

To better analyze the balance between the inertial, viscous, and interfacial forces during the bubble pinch-off process, Fig. 6 proposes cartographies of the two flow patterns by plotting of the two-phase Capillary number ($\mathrm{Ca}_{TP} = \frac{\mu_L j_{TP}}{\sigma_L}$) versus the gas-liquid superficial velocity ratio η_0, and the liquid phase Capillary number ($\mathrm{Ca}_L = \frac{\mu_L j_L}{\sigma_L}$) versus the gas phase Weber number ($\mathrm{We}_G = \frac{\rho_L {j_G}^2 d_h}{\sigma_L}$). In addition, the squeezing and dripping regimes identified from Fig. 5 were also plotted in Fig. 6 for comparison.

In Fig. 6 (a), it can be observed that at a given two-phase $\mathrm{Ca}_{\mathrm{TP}}$ number, the pinch-off pattern moved from type I to type II with increasing η_0. At a given η_0, an increase of $\mathrm{Ca}_{\mathrm{TP}}$ number turned the pinch-off pattern from type II to type I (i.e., the increase of j_{TP}). Furthermore, the dripping regimes were mainly found at low η_0 and high $\mathrm{Ca}_{\mathrm{TP}}$ number, whereas the squeezing regimes were mainly found at high η_0. These transitions between the dripping and squeezing regimes were consistent with the simulation results from Li et al. (2019). In addition, all the points corresponding to pinch-off pattern type II belonged to the squeezing regimes, while there were hybrid squeezing and dripping regimes for pinch-off pattern type I.

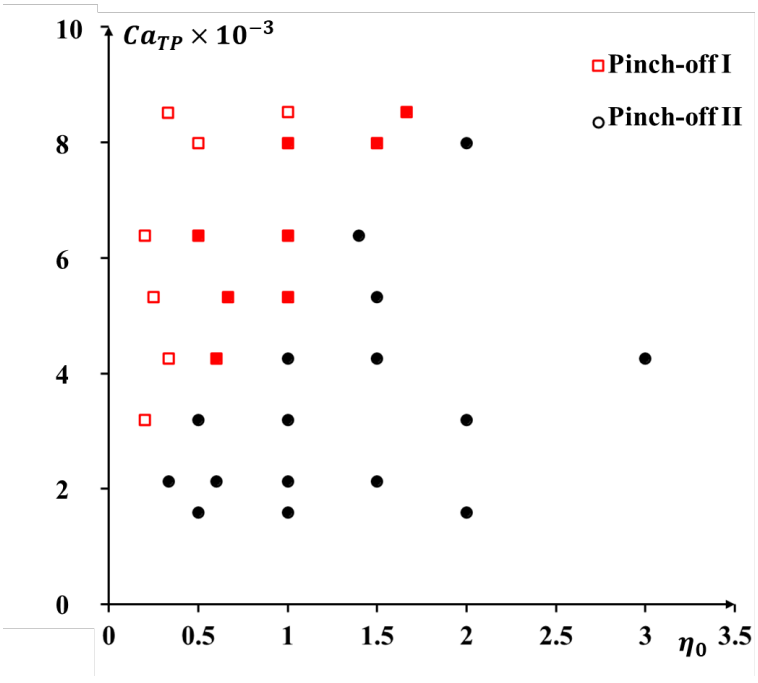

(a)

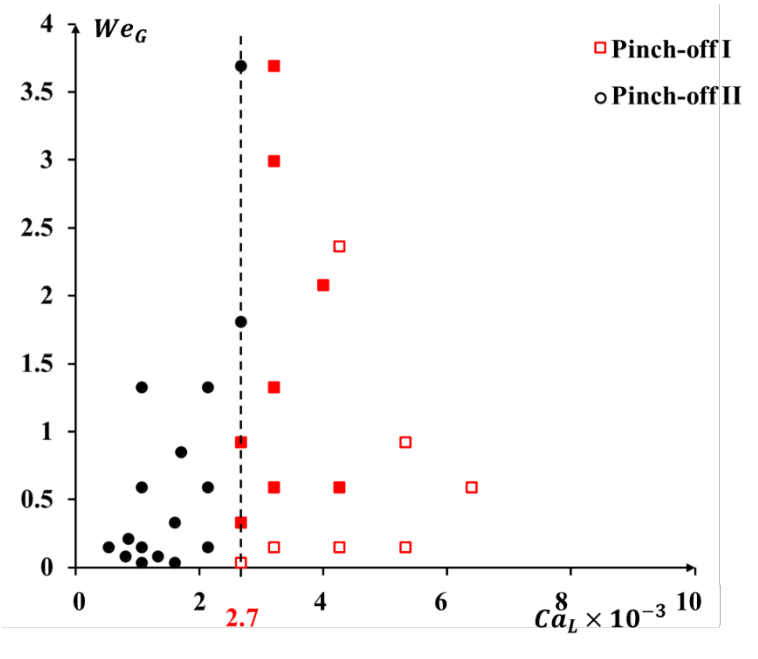

(b)

Fig. 6 Cartography of the pinch-off patterns for (a) two-phase Capillary numbers versus the gas-liquid superficial velocity ratios and (b) gas Weber numbers versus the liquid Capillary numbers. Empty and solid symbols represent dripping and squeezing regimes, respectively, for pinch-off type I (red) and pinch-off type II (black).

Fig. 6 (b) further analyzed the transitions between each regime (either dripping or squeezing) and each pinch-off pattern (either type I or type II) by plotting the gas phase Weber number and liquid phase Capillary number. It can be observed that (i) the liquid phase Capillary number Ca_L had a major impact on

the transitions between pinch-off patterns, and (ii) a critical Ca_L was found at 2.7×10^{-3}. This implies that the axial position of the bubble pinch-off was mainly controlled by the balance between the viscous force and surface tension force, and thus that higher viscous force was favorable to break up the bubble inside the cross-junction. In addition, the dripping regimes were mainly encountered at high Ca_L and low We_G number whereas the squeezing regimes were located at low Ca_L. This was also in accordance with the identified bubble formation regimes reported by Sontti and Atta (2019).

3.3 Flow regimes and bubble shape after the bubble pinch-off

After the bubble pinch-off (i.e., once the bubbles were detached), the gas-liquid flow regimes were identified. For that, various gas and liquid flow rates were considered for the air/RGN colorimetric solution, as displayed in Fig. 7. The observing position was fixed at $X_2 = 17$ mm. The observing position X represented the beginning position of the region-of-interest (ROI) window and X=0 the bubble formation position (i.e., at the cross-junction).

Fig. 7 demonstates that a small change in liquid phase properties (from deionized water to RGN colorimetric solution) induced strong differences in terms of dewetting phenomena, and thus of bubble shapes. One could also observe that:

- When $We_{TP} < 1.3$ ($Ca_{TP} < 3.2\times10^{-3}$), dewetting phenomena occurred for long bubbles.
- When $We_{TP} < 3.7$ ($Ca_{TP} < 5.3\times10^{-3}$), the bubble nose and rear were symmetrical with each other and could be described by hemispherical caps with same curvatures.
- An increase in Ca_{TP} or We_{TP} number induced bubble deformation and made bubble nose slender and bubble rear flatter. When $We_{TP} >$

8.3 (Ca_{TP} > 8.0×10^{-3}), the bubble was significantly deformed and presented like a bullet.

– At the same η_0, the increase in Ca_{TP} or We_{TP} number decreased the bubble and liquid slug lengths (Korczyk et al., 2019; Schuler et al., 2021).

Therefore, in Fig. 7, the Taylor flow regime associated with the conditions where hemispherical bubble noses and tails and moderate bubble lengths were obtained and marked by a dotted blue box. It was operated under moderate Ca_{TP} (4.3×10^{-3} - 8.0×10^{-3}) and We_{TP} (2.4 - 8.3) numbers and will be further discussed in terms of bubble and liquid slug lengths in section 3.4.

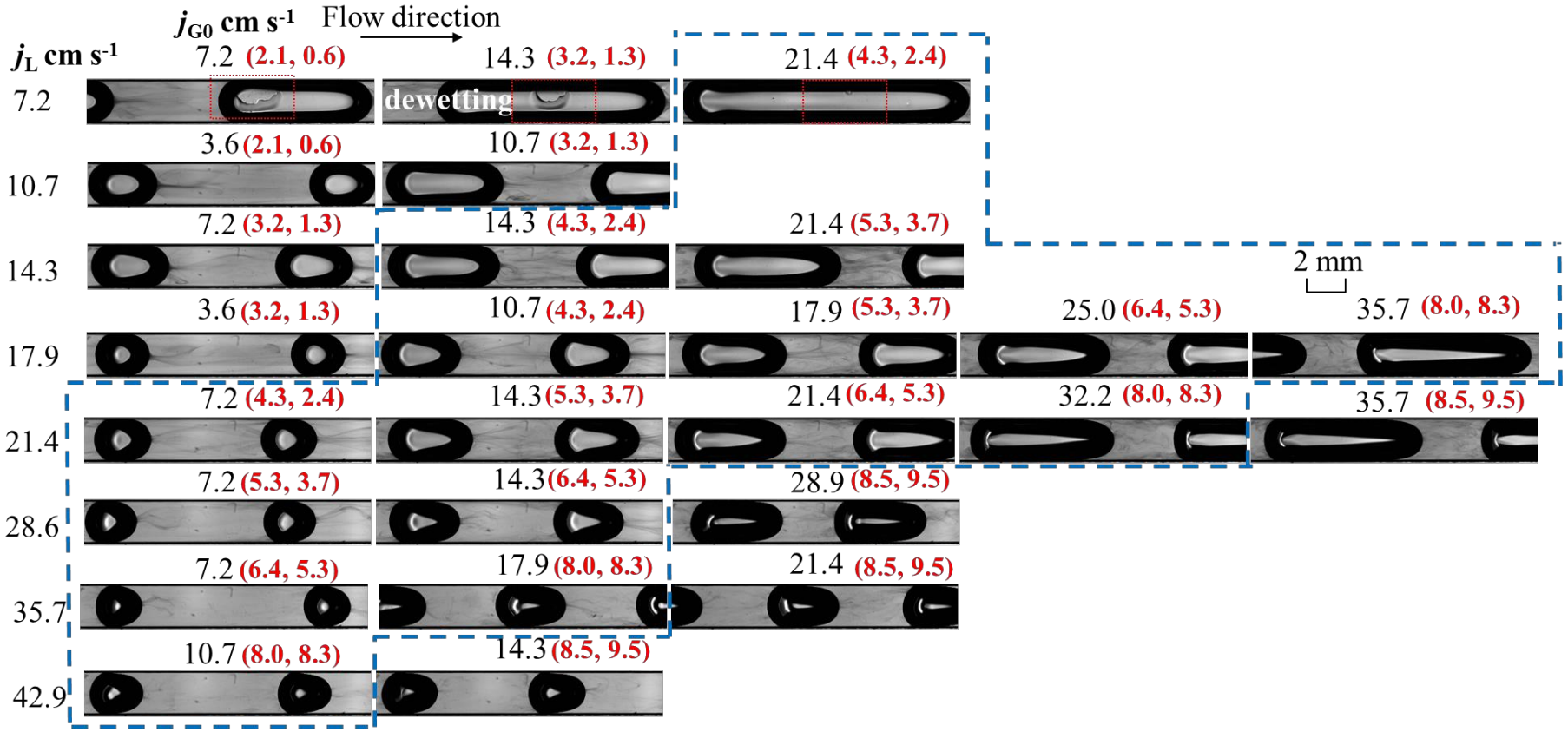

Fig. 7 Cartography of gas-liquid flows (air and RGN colorimetric solution) obtained for various operating conditions at the observing position X_2 = 17 mm. The numbers inside the red brackets correspond to ($Ca_{TP}\times10^{-3}$, We_{TP}). The dotted red boxes point out the location of wetting/dewetting phenomena. The dotted blue box corresponds to the Taylor flow regime.

3.4 Normalized bubble, liquid slug length and bubble velocity during the flowing stage

Fig. 8 (a) plots the relationships between the normalized bubble lengths with the gas-liquid superficial velocity ratios η_0, only in the case of the Taylor flow regime identified from Fig. 7 (i.e., moderate Ca_{TP} and We_{TP} numbers). Four observing positions (i.e., $X_1 / d_h = 0$, $X_6 / d_h = 52$, $X_8 / d_h = 88$ and $X_{12} / d_h = 223$) were chosen in order to cover the whole length of the milli-channel. The bubble lengths were normalized by the hydraulic diameter of the channel d_h. First, one can observe that the bubble lengths was maintained constant whatever the axial positions X, indicating that the pressure drop was small, and the expansion effect of gas phase was negligible here. In addition, the normalized bubble length could be predicted using the scaling law proposed by Garstecki et al. (2006) (initially proposed for T-junction), as follows:

$$\frac{L_B}{d_h} = 1 + 1.83\,\eta_0, \qquad \text{MAPER: } 4.4\% \tag{4}$$

where MAPER is the Mean Absolute Percentage Error of Regression, defined in the Supplementary Material S4.

As proposed by Abadie (2013), the bubble length can be analyzed from the characteristic times defined in section 3.1, as below:

$$t_{filling} \cong \frac{d_h}{U_{filling}} \cong \frac{d_h}{j_{G0}} \tag{5}$$

where the filling velocities of the gas phase, $U_{filling}$, is proportional to the gas superficial velocities.

$$t_{squeezing} \cong \frac{w_{squeezing}}{U_{squeezing}} \cong \frac{w_{squeezing}}{j_L} \tag{6}$$

where $w_{squeezing}$ is defined as the squeezing length for the liquid phase to break up the gas phase.

As the bub ble formation time, t_{BF}, is the inverse of the bubble formation frequency f_{BF}, the following equation could be also obtained from Eq. (3):

$$t_{BF} \cong \frac{L_B}{U_{BF}} \cong \frac{L_B}{j_{G0}} \tag{7}$$

At last, by combining Eqs. (5) to (7) and replacing them in Eq. (1), the bubble length could be correlated as:

$$\frac{L_B}{d_h} \cong 1 + \frac{w_{squeezing}}{d_h}\frac{j_G}{j_L} = 1 + \frac{w_{squeezing}}{d_h}\eta_0 \tag{8}$$

In Eq. (4) deduced from experimental data (Fig. 8 (a)), a value of one as intercept was also obtained, confirming that, in the present case, the bubble formation could be described with both filling and squeezing stages. The comparison between Eqs. (4) and (8) would also suggest that the squeezing length for the liquid phase to break up the gas phase, $w_{squeezing}$, was 1.83 times of the channel hydraulic diameter d_h. Note that this value of 1.83 was in accordance with the ones obtained by Yang (2017), in the straight channel (1.58) and in the meandering channel (1.69).

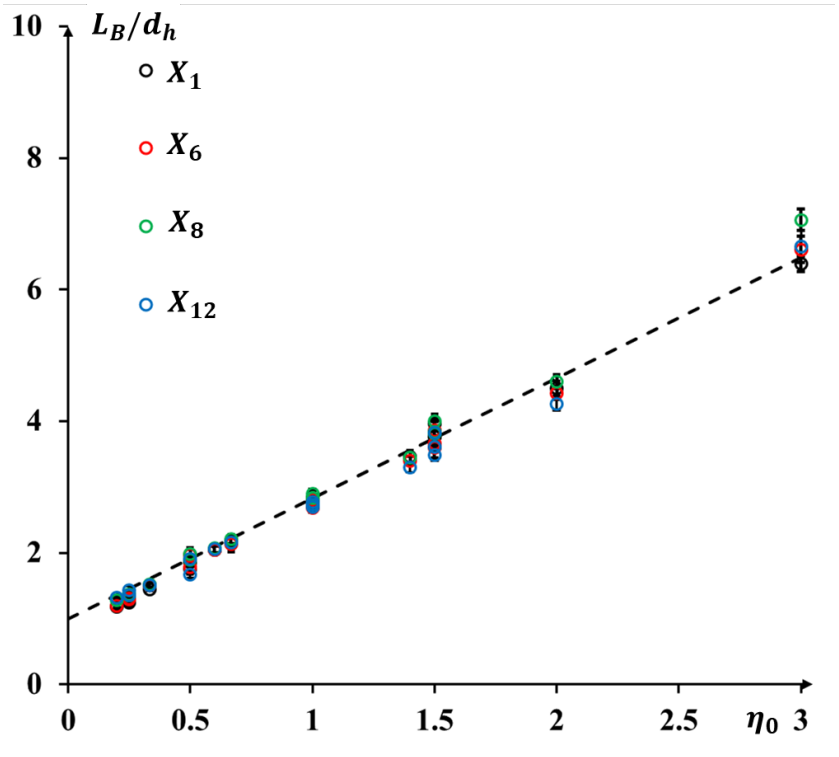

(a)

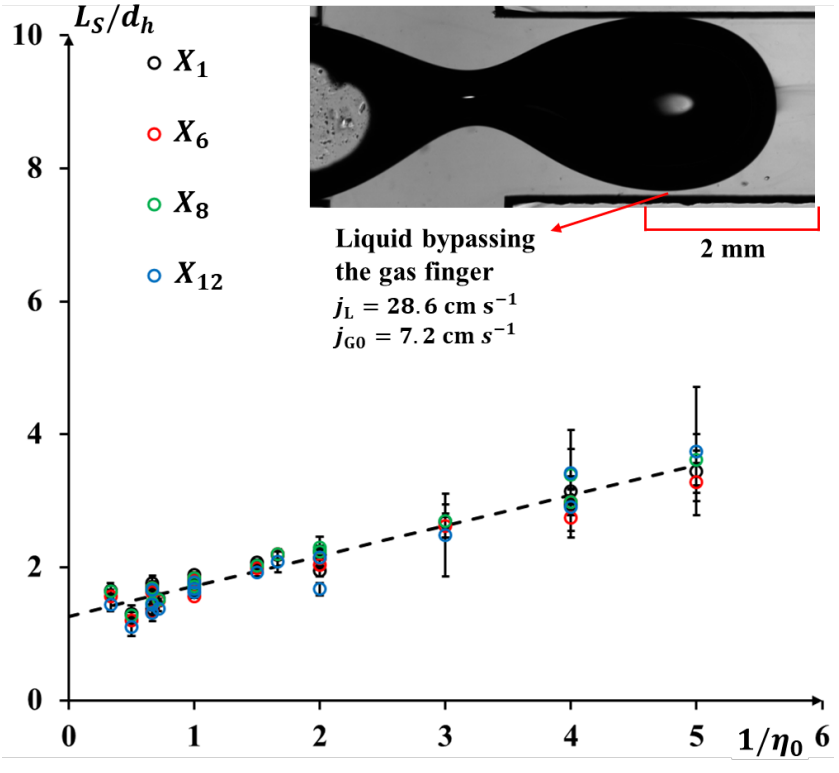

(b)

Fig. 8 Flowing stage: (a) normalized bubble length versus the gas-liquid ratio η_0, (b) normalized liquid slug length versus the inverse of η_0. Four observing ROI positions ($X_1 / d_h = 0$, $X_6 / d_h = 52$, $X_8 / d_h = 88$, $X_{12} / d_h = 223$) and four groups of two-phase superficial velocities ($j_{TP} = 28.6$, 35.7, 42.9, 53.6 cm s^{-1}) were considered.

It can be observed that, from Eq. (3), the ratio ϖ between the bubble volume and the channel volume occupied by the same length of the bubble could be directly deduced, knowing the bubble formation frequency and bubble length (see in Table S4 of Supplementary Material S5). It is found that ϖ ranged from 0.5 to 1.0 and increased with the gas-liquid superficial velocity ratio η_0.

Fig. 8 (b) plots the relationships between the normalized liquid slug lengths and the inverse of η_0. Unlike the cases of L_B, the standard deviations of normalized liquid slug length were relatively higher when $1/\eta_0$ was higher than 2. As illustrated by the image (right before the bubble pinch-off) inserted in Fig. 8 (b), these conditions corresponded to the cases (identified to the dripping regimes) where the channel was not fully blocked by the bubble and so, the coming liquid could freely enter into the liquid slug and bypass the gas thread. Under such dripping regime, the pinch-off became triggered by the viscous and inertial forces, and no more by the increased pressure force induced at the upstream of the gas thread as for the squeezing regimes (Schuler et al., 2021).

The normalized liquid slug length could be described by the following scaling law under the Taylor flow regime identified from Fig. 7 as well:

$$\frac{L_S}{d_h} = 1.26 + \frac{0.46}{\eta_0}, \qquad \text{MAPER: 7.6\%} \tag{9}$$

The bubble length relative to the unit cell length, ψ, was defined in the following equation:

$$\psi = L_B/(L_B+L_S) \tag{10}$$

The axial positions and the gas and liquid flow rates had no effect on the variations of ψ. A shown in Fig. 9, with increasing η_0, ψ increased significantly as observed in the in-plane spiral-shaped milli-reactor (Mei et al., 2020). Martin et al. (2018) and Abadie (2013) proposed to describe the variation of the bubble length relative to the unit cell length by the following relation

$$\Psi = \frac{\eta_0}{\eta_0+\alpha} \tag{11}$$

where α is a constant.

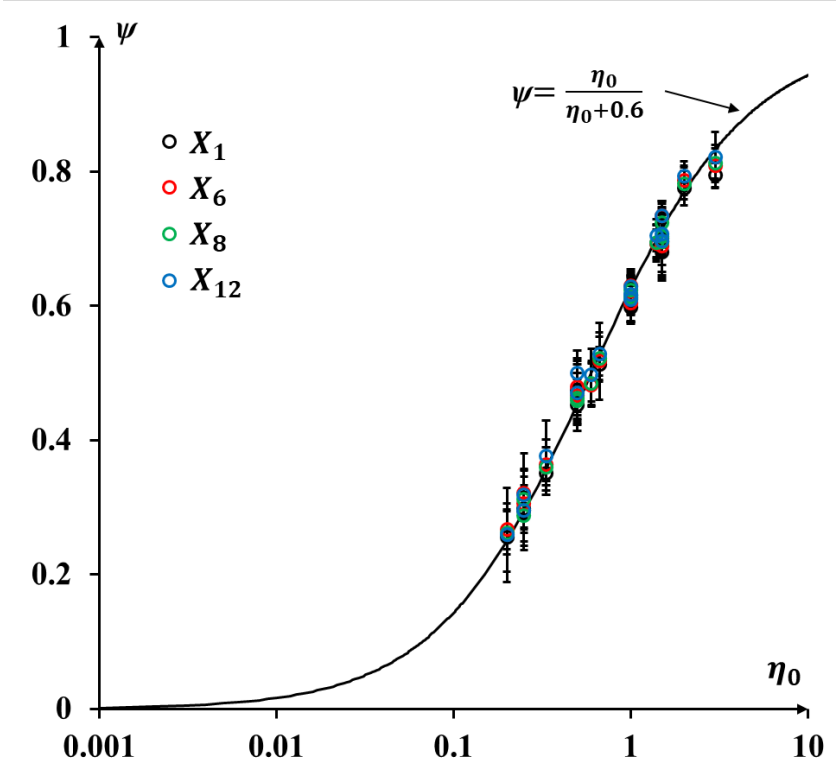

Fig. 9 Normalized unit cell length versus η_0 during flowing stage. Four observing ROI positions ($X_1/d_h = 0$, $X_6/d_h = 52$, $X_8/d_h = 88$, $X_{12}/d_h = 223$) and four groups of two-phase superficial velocities ($j_{TP} = 28.6, 35.7, 42.9, 53.6$ cm s^{-1}) were considered.

Fig. 9 demonstrated that this equation is fully relevant for modeling the present experiments and the fitted constant α was equal to 0.6, in accordance with the study by Abadie (2013), in which the gas-liquid flow was formed by a cross-junction as well.

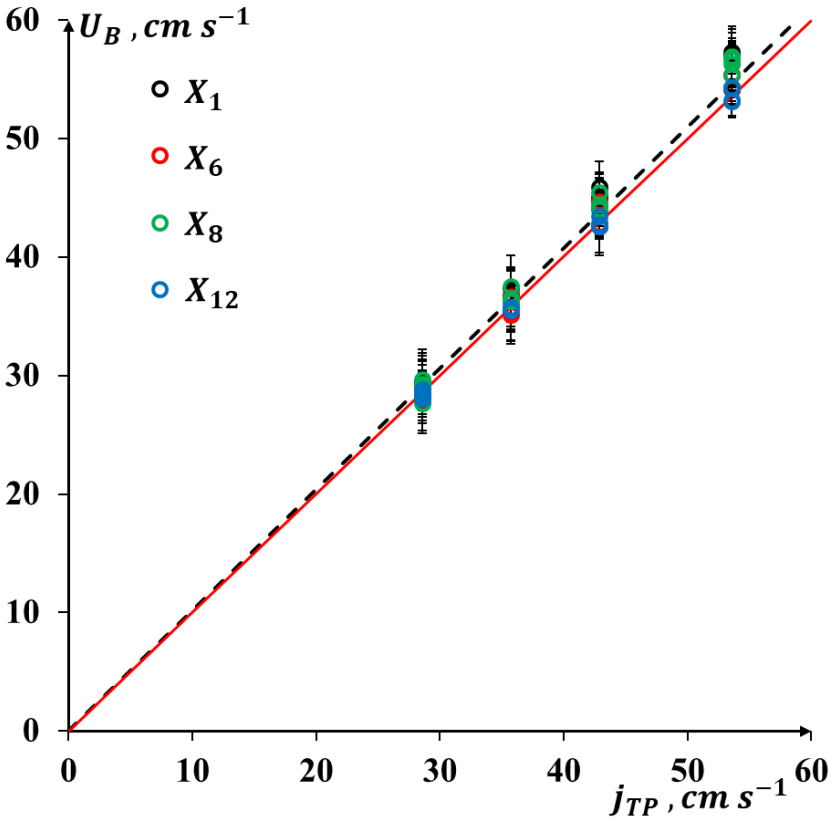

Fig. 10 Bubble velocities versus two-phase superficial velocities for four observing positions ($X_1 / d_h = 0$, $X_6 / d_h = 52$, $X_8 / d_h = 88$, $X_{12} / d_h = 223$).

At last, Fig. 10 compares the bubble velocities with the two-phase superficial velocities for different observing positions. The bubble velocities could be described by the drift flux model as below:

$$U_B = 1.02\, j_{TP}, \qquad \text{MAPER: } 2.0\% \tag{12}$$

Eq. (12) would suggest that the bubbles traveled at a velocity almost equal to the two-phase superficial velocities. Note that the bubble velocities remained constant whatever the axial positions in the straight milli-channel.

All the obtained bubble length, liquid slug length and the bubble velocity are summarized in the Supplementary Material S5.

4. Conclusions

The dynamics of bubble formation was investigated at a cross-junction in a straight millimetric channel, as well as the dynamics after the bubble pinch-off (i.e., bubble flowing stage). The main findings were as follows:

1) The bubble formation broadly consisted of gas filling and liquid squeezing stages, and the related frequencies were mainly controlled by the gas and liquid superficial velocities, respectively.

2) Based on the measurements of the gas finger length (normalized by the width of side channel), two types of bubble pinch-off patterns were identified. The transition between them could be determined by a critical liquid Capillary number at 2.7×10^{-3}. The squeezing and dripping regimes of bubble formation were also characterized in terms of gas Weber number and liquid Capillary numbers.

3) Once the bubbles detached, gas-liquid flow regimes were described, and Taylor flow regime identified under moderate Ca_{TP} ($4.3 - 8.0\times10^{-3}$) and We_{TP} (2.4 - 8.3) numbers. In addition, some dewetting phenomena of lubrication liquid film were observed when $We_{TP} < 1.3$. Bubble shapes were affected by increasing Ca_{TP} or We_{TP}, the bubble nose and bubble rear becoming slender and flatter respectively.

4) In the Taylor flow regime, the bubble and liquid slug lengths could be described by the scaling laws based on the gas-liquid superficial velocity ratio and the inverse of it, respectively. A mathematical relationship was also proposed to describe the variation of the bubble length relative to the unit cell length with the gas-liquid superficial velocity ratio as well.

At last, this works allowed getting quantitative characterisation of the dynamics during and right after the bubble formation, and thus achieving a better understanding on the underlying mechanisms. This will serve as basis for investigating the gas-liquid mass transfer occurring during these earlier stages, as presented in the Part 2 of the present paper.

Acknowledgments

The author would like to acknowledge the financial assistance provided by the China Scholarship Council. We also acknowledge the support for this work from the CNRS research federation FERMaT.

Nomenclature

Latin letters

Symbol	Description	SI Units
d_h	Channel hydraulic diameter	[m]
f_{BF}	Bubble formation frequency	[s^{-1}]
$f_{filling}$	Frequency of gas filling during bubble formation	[s^{-1}]
$f_{squeezing}$	Frequency of liquid squeezing during bubble formation	[s^{-1}]
j_{G0}	Superficial velocity of the gas phase ($j_{G0} = Q_{G0}/\Omega$)	[$m{\cdot}s^{-1}$]
j_L	Superficial velocity of the liquid phase ($j_L = Q_L/\Omega$)	[$m{\cdot}s^{-1}$]
j_{TP}	Total superficial velocity for two-phase flow ($j_{TP}=j_{G0}+j_L$)	[$m{\cdot}s^{-1}$]
L_B	Bubble length	[m]
l_{GF}	Gas finger length right after bubble pinch-off	[m]
L_S	Liquid slug length	[m]
Q	Volumetric flow rate	[$m^3\ s^{-1}$]
U_B	Bubble velocity	[$m\ s^{-1}$]
t	Time	[s]
$t_{filling}$	Gas filling time during bubble formation	[s]
$t_{squeezing}$	Liquid squeezing time during bubble formation	[s]
t_{BF}	Bubble formation time	[s]
w_{side}	Horizontal width of the liquid inlet side channel	[m]
X	Axial position along the spiral tube from the bubble formation point	[m]
x	x axis in Cartesian coordinates	[m]
y	y axis in Cartesian coordinates	[m]
z	z axis in Cartesian coordinates	[m]

Greek symbols

η_0	Ratio of the superficial velocities of the gas and the liquid phases at the inlet of the channel ($\eta_0 = j_{G0} / j_L$)	[-]
μ	Dynamic viscosity of the phase	[Pa s]
Ω	Cross-sectional area of the channel ($\Omega = {d_h}^2$)	[m^2]
ϖ	The ratio between the bubble volume to the channel volume occupied by the same length of the bubble	[-]
ρ	Density of the phase	[kg m^{-3}]
σ_L	Surface tension of the liquid phase	[N m^{-1}]
ψ	Bubble length relative to the unit cell, defined as $\psi = \frac{L_B}{L_{UC}}$	[-]

Dimensionless numbers

Two-phase Capillary number	$\mathrm{Ca}_{TP} = \frac{\mu_L j_{TP}}{\sigma_L}$
Liquid Capillary number	$\mathrm{Ca}_L = \frac{\mu_L j_L}{\sigma_L}$
Two-phase Weber number	$\mathrm{We}_{TP} = \frac{\rho_L {j_{TP}}^2 d_h}{\sigma_L}$
Gas Weber number	$\mathrm{We}_G = \frac{\rho_L {j_G}^2 d_h}{\sigma_L}$

Abbreviations

fps	Frames per second

GL	Glucose
LED	Light-emitting diode
MAPER	Mean absolute percentage error of regression
PMMA	Poly-Methyl-Methacrylate
ROI	Region-of-interest
RZ	Resazurin
RF	Resorufin
RGN	Resazurin, Glucose, NaOH colorimetric solution

Subscripts and Superscripts

B	Bubble
G	Gas phase
L	Liquid phase
TP	Two-phase flow
UC	Unit cell

Declaration of Competing Interest

The authors report no declarations of interest.

REFERENCES

Abadie, T., 2013. Hydrodynamics of gas-liquid Taylor flow in microchannels. École Doctorale Mécanique, Énergétique, Génie civil et Procédés, Toulouse, INP.

Castro-Hernández, E., Van Hoeve, W., Lohse, D., Gordillo, J.M., 2011. Microbubble generation in a co-flow device operated in a new regime. Lab on a Chip - Miniaturisation for Chemistry and Biology 11, 2023-2029. https://doi.org/10.1039/c0lc00731e

Dang, M., Yue, J., Chen, G., Yuan, Q., 2013. Formation characteristics of Taylor bubbles in a microchannel with a converging shape mixing junction. Chemical Engineering Journal 223, 99-109. https://doi.org/10.1016/j.cej.2013.02.108

De Menech, M., Garstecki, P., Jousse, F., Stone, H.A., 2008. Transition from squeezing to dripping in a microfluidic T-shaped junction. Journal of Fluid Mechanics 595, 141-161.

Dietrich, N., Poncin, S., Midoux, N., Li, H.Z., 2008. Bubble formation dynamics in various flow-focusing microdevices. Langmuir 24, 13904-13911. https://doi.org/10.1021/la802008k

Dietrich, N., Loubière, K., Jimenez, M., Hébrard, G., Gourdon, C., 2013. A new direct technique for visualizing and measuring gas–liquid mass transfer around bubbles moving in a straight millimetric square channel. Chemical Engineering Science 100, 172-182. https://doi.org/10.1016/j.ces.2013.03.041

Dollet, B., Van Hoeve, W., Raven, J.-P., Marmottant, P., Versluis, M., 2008. Role of the channel geometry on the bubble pinch-off in flow-focusing devices. Physical Review Letters 100, 034504.

Fu, T., Ma, Y., Funfschilling, D., Li, H.Z., 2009. Bubble formation and breakup mechanism in a microfluidic flow-focusing device. Chemical Engineering Science 64, 2392-2400. https://doi.org/10.1016/j.ces.2009.02.022

Fu, T., Funfschilling, D., Ma, Y., Li, H.Z., 2010a. Scaling the formation of slug bubbles in microfluidic flow-focusing devices. Microfluidics and Nanofluidics 8, 467-475. https://doi.org/10.1007/s10404-009-0471-0

Fu, T., Ma, Y., Funfschilling, D., Zhu, C., Li, H.Z., 2010b. Squeezing-to-dripping transition for bubble formation in a microfluidic T-junction. Chemical Engineering Science 65, 3739-3748. https://doi.org/10.1016/j.ces.2010.03.012

Fu, T., Ma, Y., Funfschilling, D., Li, H.Z., 2011. Dynamics of bubble breakup in a microfluidic T-junction divergence. Chemical Engineering Science 66, 4184-4195. https://doi.org/10.1016/j.ces.2011.06.003

Fu, T., Ma, Y., Funfschilling, D., Zhu, C., Li, H.Z., 2012. Breakup dynamics of slender bubbles in non-newtonian fluids in microfluidic flow-focusing devices. AIChE Journal 58, 3560-3567. https://doi.org/10.1002/aic.13723

Fu, T., Ma, Y., 2015. Bubble formation and breakup dynamics in microfluidic devices: A review. Chemical Engineering Science 135, 343-372. https://doi.org/10.1016/j.ces.2015.02.016

Garstecki, P., Stone, H.A., Whitesides, G.M., 2005. Mechanism for flow-rate controlled breakup in confined geometries: A route to monodisperse emulsions. Physical Review Letters 94, 164501.

Garstecki, P., Fuerstman, M.J., Stone, H.A., Whitesides, G.M., 2006. Formation of droplets and bubbles in a microfluidic T-junction - scaling and mechanism of break-up. Lab on a Chip 6, 437-446. https://doi.org/10.1039/b510841a

Geng, Y., Ling, S., Huang, J., Xu, J., 2020. Multiphase Microfluidics: Fundamentals, Fabrication, and Functions. Small 16, e1906357. https://doi.org/10.1002/smll.201906357

Haase, S., 2017. Characterisation of gas-liquid two-phase flow in minichannels with co-flowing fluid injection inside the channel, part II: gas bubble and liquid slug lengths, film thickness, and void fraction within Taylor flow. International Journal of Multiphase Flow 88, 251-269. https://doi.org/https://doi.org/10.1016/j.ijmultiphaseflow.2016.09.002

Korczyk, P.M., van Steijn, V., Blonski, S., Zaremba, D., Beattie, D.A., Garstecki, P., 2019. Accounting for corner flow unifies the understanding of droplet formation in microfluidic channels. Nature Communications 10, 2528.

Li, X., He, L., He, Y., Gu, H., Liu, M., 2019. Numerical study of droplet formation in the ordinary and modified T-junctions. Physics of Fluids 31, 082101.

Li, X., Huang, Y., Chen, X., Sunden, B., Wu, Z., 2020. Breakup dynamics of gas-liquid interface during Taylor bubble formation in a microchannel flow-focusing device. Experimental Thermal and Fluid Science 113, 110043. https://doi.org/10.1016/j.expthermflusci.2020.110043

Li, X., Wu, Z., Chen, X., 2021. Analysis on breakup dynamics of hydrogen taylor bubble formation in a cross-junction microchannel. International Journal of Hydrogen Energy 46, 33438-33452. https://doi.org/https://doi.org/10.1016/j.ijhydene.2021.07.178

Liu, H., Zhang, Y., 2011. Droplet formation in microfluidic cross-junctions. Physics of Fluids 23, 082101. https://doi.org/10.1063/1.3615643

Lu, Y., Fu, T., Zhu, C., Ma, Y., Li, H.Z., 2014a. Scaling of the bubble formation in a

flow-focusing device: Role of the liquid viscosity. Chemical Engineering Science 105, 213-219. https://doi.org/10.1016/j.ces.2013.11.017

Lu, Y., Fu, T., Zhu, C., Ma, Y., Li, H.Z., 2014b. Pinch-off mechanism for Taylor bubble formation in a microfluidic flow-focusing device. Microfluidics and Nanofluidics 16, 1047-1055. https://doi.org/10.1007/s10404-013-1274-x

Madana, V.S.T., Ali, B.A., 2020. Numerical investigation of engulfment flow at low Reynolds numbers in a T-shaped microchannel. Physics of Fluids 32, 072005. https://doi.org/10.1063/5.0013957

Martin, A., Camy, S., Aubin, J., 2018. Hydrodynamics of CO2-ethanol flow in a microchannel under elevated pressure. Chemical Engineering Science 178, 297-311. https://doi.org/https://doi.org/10.1016/j.ces.2017.12.046

Mei, M., Felis, F., Dietrich, N., Hébrard, G., Loubière, L., 2020. Hydrodynamics of gas-liquid slug flows in a long in-plane spiral-shaped milli-reactor. Theoretical Foundations of Chemical Engineering 54, 25-47. https://doi.org/10.1134/S0040579520010169

Otsu, N., 1979. A threshold selection method from gray-level histograms. IEEE transactions on systems, man, and cybernetics 9, 62-66.

Schuler, J., Neuendorf, L.M., Petersen, K., Kockmann, N., 2021. Micro-computed tomography for the 3D time-resolved investigation of monodisperse droplet generation in a co-flow setup. AIChE Journal 67. https://doi.org/10.1002/aic.17111

Shao, N., Salman, W., Gavriilidis, A., Angeli, P., 2008. CFD simulations of the effect of inlet conditions on Taylor flow formation. International Journal of Heat and Fluid Flow 29, 1603-1611.

Sontti, S.G., Atta, A., 2019. Numerical insights on controlled droplet formation in a microfluidic flow-focusing device. Industrial & Engineering Chemistry Research 59, 3702–3716.

Sontti, S.G., Pallewar, P.G., Ghosh, A.B., Atta, A., 2019. Understanding the Influence of Rheological Properties of Shear-Thinning Liquids on Segmented Flow in Microchannel using CLSVOF Based CFD Model. The Canadian Journal of Chemical Engineering 97, 1208-1220. https://doi.org/https://doi.org/10.1002/cjce.23391

Svetlov, S.D., Abiev, R.S., 2021. Mathematical modeling of the droplet formation process in a microfluidic device. Chemical Engineering Science, 116493. https://doi.org/10.1016/j.ces.2021.116493

Van Hoeve, W., Dollet, B., Versluis, M., Lohse, D., 2011. Microbubble formation and pinch-off scaling exponent in flow-focusing devices. Physics of Fluids 23, 092001.

Xu, F., Yang, L., Liu, Z., Chen, G., 2021. Numerical investigation on the

hydrodynamics of Taylor flow in ultrasonically oscillating microreactors. Chemical Engineering Science, 116477. https://doi.org/10.1016/j.ces.2021.116477

Xu, J.H., Li, S., Tan, J., Luo, G., 2008. Correlations of droplet formation in T-junction microfluidic devices: from squeezing to dripping. Microfluidics and Nanofluidics 5, 711-717.

Xu, K., Tostado, C.P., Xu, J.H., Lu, Y.C., Luo, G.S., 2014. Direct measurement of the differential pressure during drop formation in a co-flow microfluidic device. Lab on a Chip 14, 1357.

Yang, L., 2017. Local investigations of gas-liquid mass transfer around Taylor bubbles flowing in straight and meandering millimetric channels using a colorimetric method. Toulouse, INSA.

Yao, C., Zhao, Y., Ma, H., Liu, Y., Zhao, Q., Chen, G., 2021. Two-phase flow and mass transfer in microchannels: A review from local mechanism to global models. Chemical Engineering Science 229, 116017. https://doi.org/https://doi.org/10.1016/j.ces.2020.116017

Zhang, C., Fu, T., Zhu, C., Jiang, S., Ma, Y., Li, H.Z., 2017. Dynamics of bubble formation in highly viscous liquids in a flow-focusing device. Chemical Engineering Science 172, 278-285. https://doi.org/10.1016/j.ces.2017.06.026

Graphical Abstract:

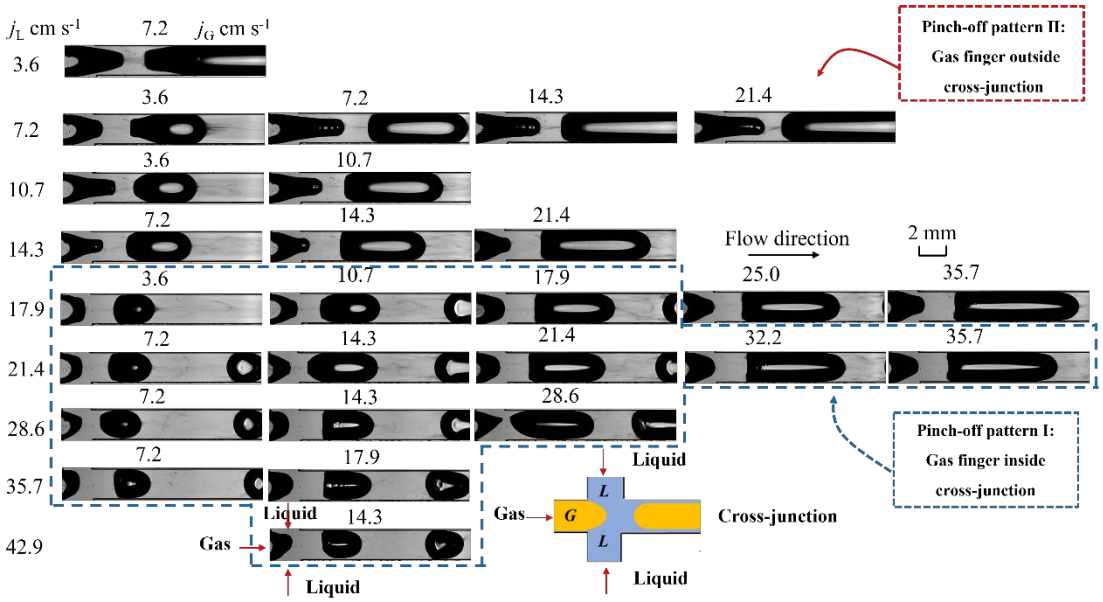

Taylor bubble formation and flowing in a straight millimetric channel with a cross-junction inlet geometry

Part I: Bubble dynamics

Mei Mei[1,2,3], Claude Le Men[1,3], Karine Loubière[2,3], Gilles Hébrard[1,3], Nicolas Dietrich[1*,3]

[1] Toulouse Biotechnology Institute, Université de Toulouse, CNRS, INRAE, INSA, Toulouse, France

[2] Laboratoire de Génie Chimique, Université de Toulouse, CNRS, INP, UPS, Toulouse, France

[3] Fédération de Recherche FERMAT, CNRS, Toulouse, France

*Corresponding author: Dr. Nicolas Dietrich

E-mail: nicolas.dietrich@insa-toulouse.fr

S1 Calibration of the channel depth at the cross-junction of the straight millimetric channel

As shown in Fig. S 1, all the channels, including the injection inlets of gas and liquid, and the main channel, were designed to have the same square cross-section ($w^2 \cong 2\times2$ mm^2). However, it was observed that these dimensions could slightly deviate from 2 mm due to the manufacturing precision and mounting deformation of the channel. As involved in all the calculations for hydrodynamics and mass transfer (Parts I and II of the article), it was necessary to determine their exact values. A specific method was developed for the depth of the main channel, w_v, while the side channel and main channel widths, w_{side} and w_h, were calibrated by a micro-ruler (0.10 mm), and found at 2.17 and 2.19 mm, respectively.

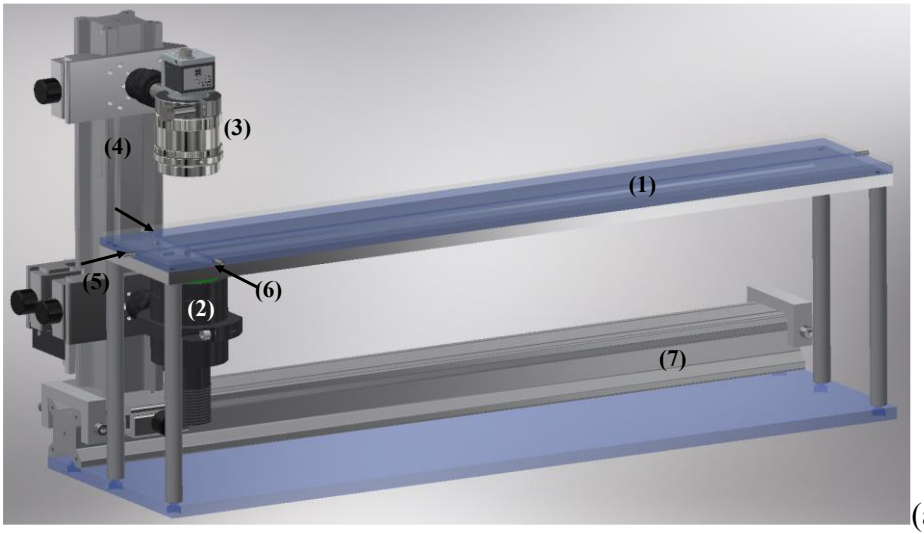

(a)

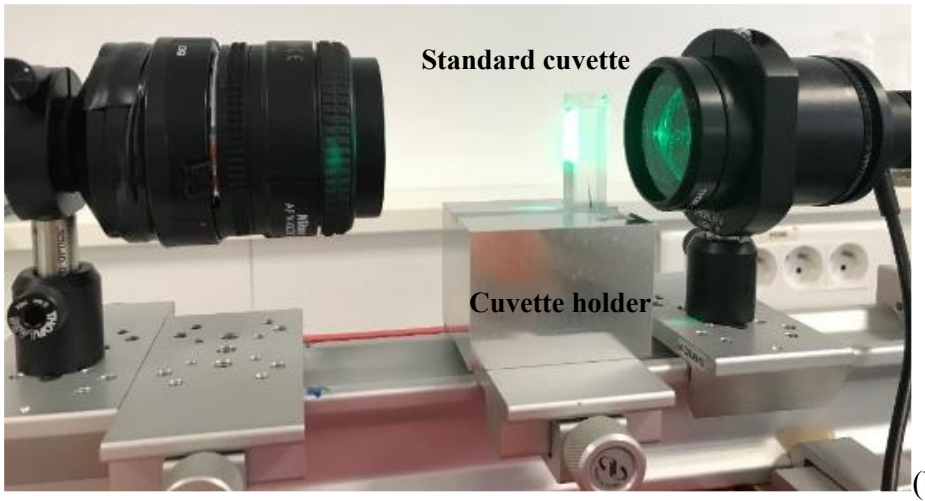

(b)

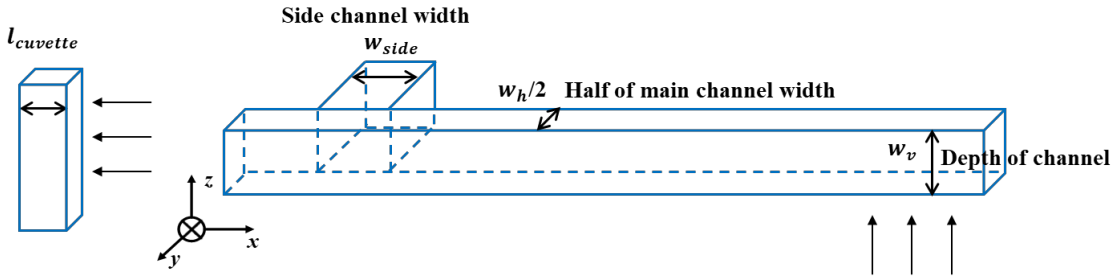

(c)

Fig. S 1 (a) Schematic representation of the experimental setup (the system I): (1) the millimetric channel (2) the backlight panel (3) high-speed camera (4) support of camera and backlight (5) gas inlet (6) liquid inlet (7) sliding support; (b) photography of the modified experimental setup (system II) involving the spectrophotometer cuvette; (c) schematic representation of the dimensions involved in the cuvette and in the channel (half of the straight channel with cross-junction is plotted for visualization convenience).

To access w_v, the experimental set-up presented in the paper (Fig. 1) was modified. As shown in Fig. S 1 (a), the camera and backlight with the supporting device (4) were removed together from sliding support (7) and put into the horizontal direction. A cell holder with a standard spectrophotometric cuvette (1 cm of optical path length) was fixed in the place of the milli-channel. Fig. S 1 (b) shows the picture of this modified experimental setup. For convenience, the milli-channel system shown in

Fig. S 1 (a) and the cuvette system shown in Fig. S 1 (b) were defined as system (I) and system (II).

The channel depth could be calibrated by means of a standard cuvette using the same optical system. According to the Beer-Lambert law (note that, thanks to the aspheric condenser lens and to the NE2R10A absorptive ND filter, the light passing through the channel could be considered almost parallel and monochromatic), the absorbance of resorufin A_{RF} could be expressed as below,

$$A_{RF} = \varepsilon\, l\, c \qquad \text{(S 1)}$$

where l, was the optical path length, ε (L mol^{-1} cm^{-1}) the molar attenuation coefficient of the resorufin dye (RF), which is the single absorbing species, and c (mol^{-1} L), the related molar concentration.

Thus, using the same dye and optical system, the optical path length in the milli-channel system (I) could be deduced from the optical path length in the cuvette system (II), according to the following equation:

$$\frac{\ell_{II}}{\ell_I} = \frac{A_{II}}{c_{II}} \times \frac{c_I}{A_I} = \frac{\Upsilon(\mathrm{II})}{\Upsilon(\mathrm{I})} \qquad \text{(S 2)}$$

where Υ was a coefficient linked to for A and c, defined for each system, and c_I and c_{II} the molar concentrations of RF used in the systems I and II respectively.

In Fig. S 1 (c), the light paths in the two systems were illustrated, as well as the different channel widths. The light paths l_{I} and l_{II} for system I and II in Eq. (S 2) corresponded to the channel depth w_{v} and the cuvette optical path l_{cuvette}, respectively.

Aqueous solutions of resorufin consisted of resazurin dye (Sigma Aldrich, CAS 199303, purity 93%, molar mass: 229.19 g mol^{-1}), glucose, and NaOH. A second dye, safranin (Sigma Aldrich, S8884, purity 80%, molar mass: 350.84 g mol^{-1}), was prepared using only deionized water (i.e., without glucose and NaOH) in order to verify the data obtained with aqueous solutions of resorufin. The resorufin aqueous solution was prepared according to the procedure established by Mei et al. (2020). Therefore, D-glucose anhydrous (Sigma Aldrich, CAS 50-99-7) and NaOH (Sigma Aldrich, CAS 1310-73-2) were both at a concentration of 20 g L^{-1}. In presence of glucose and NaOH, resazurin (blue and not fluorescent) was irreversibly converted into resorufin (pink and highly fluorescent).

The absorption spectra of resorufin- and safranin-based aqueous solutions (see Fig. S 2) were measured by a Jasco V-630 spectrophotometer. Fig. S 3 (a) presents the measured absorption spectra for resorufin. It can be observed that the maximal absorption peak was in the visible domain, at 570 nm, which was consistent with the values reported in the literature (Zrimšek et al., 2004; Doneux et al., 2016). For safranin, the absorption spectrum was characterized by a peak located at the wavelength near 530

nm, as shown in Fig. S 3 (b). For both dyes, the absorbance values *A* logically increased with the increase of concentrations.

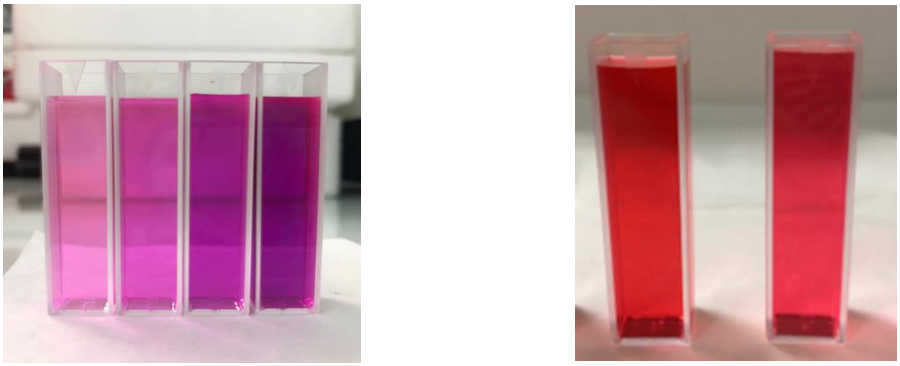

(a) (b)

Fig. S 2 Aqueous solutions of (a) resorufin, (b) safranin in the cuvette at different concentrations.

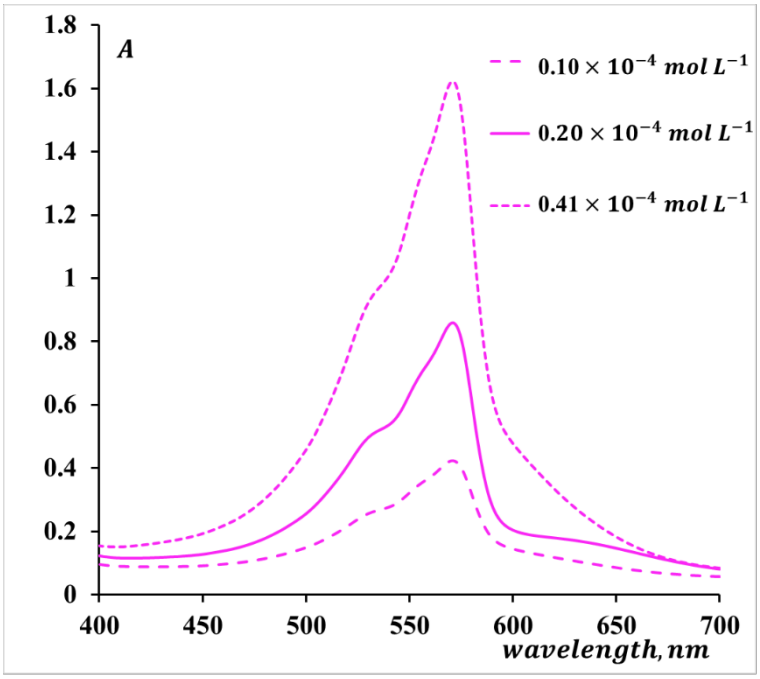

(a)

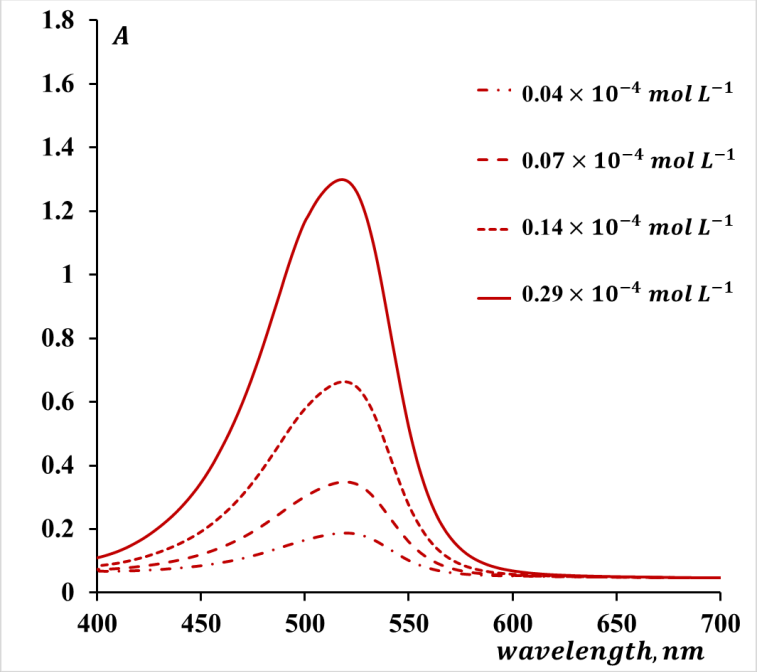

(b)

Fig. S 3 Absorbance spectra of (a) resorufin, (b) safranin aqueous solutions at different concentrations.

Table S 1 summarized the molar concentrations of safranin and resorufin dyes applied in the cuvette and milli-channel system, respectively.

Table S 1 Calibration of the channel depth (w_v) in the cross-junction device: concentrations of safranin and resorufin used in the experiments with the cuvette and the millimetric channel systems.

Dye	System	Concentrations×10^{-4} (mol L^{-1})			
Safranin	Cuvette (II)	0.04	0.07	0.14	0.29
Safranin	Milli-channel (I)	0.14	0.29	0.57	1.14
Resorufin	Cuvette (II)	0.10	0.20	0.41	/
Resorufin	Milli-channel (I)	0.41	0.81	1.62	3.25

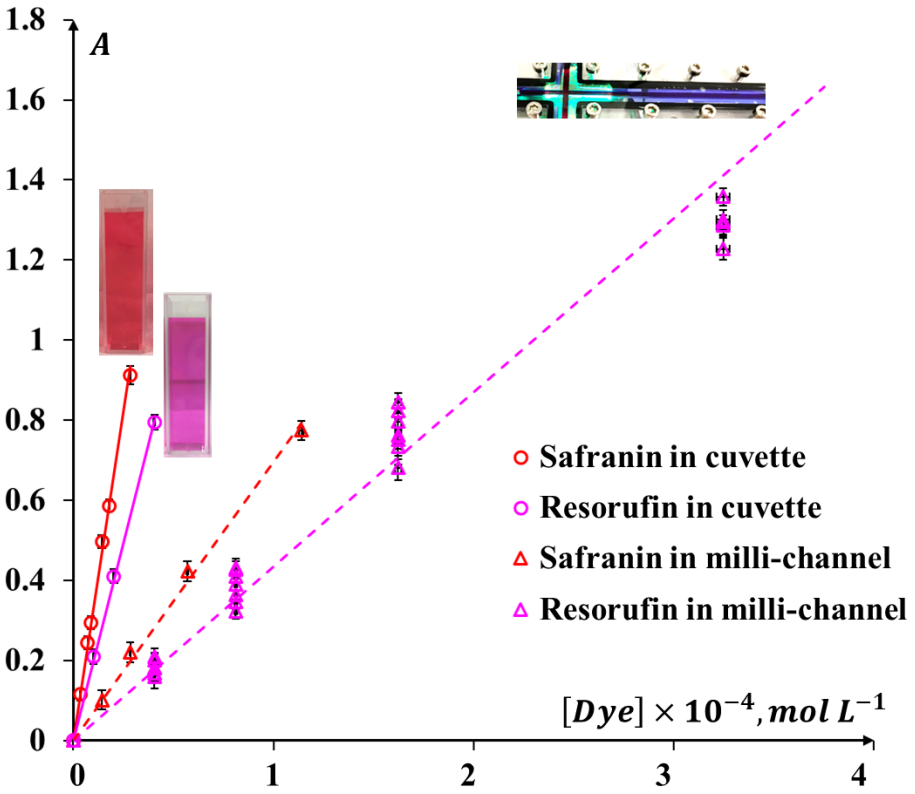

Fig. S 4 Calibration of the channel depth in the cross-junction device: relations between absorbance and concentrations of two dyes (resorufin and safranin) in the cuvette or milli-channel systems.

Fig. S 4 shows the relations between the absorbances and the concentrations of two dyes, respectively, marked by red and pink colors.

- The red and pink circular symbols correspond to the cuvette system (II).
- The red triangular symbols correspond to the millimetric channel system (I) with the safranin dye and considering the first ROI position X_1.

- The pink triangular symbol corresponds to the millimetric channel system (I) with the resorufin dye and considering different ROI positions.

According to Eq. (S 2) and from the relations illustrated in Fig. S 4, the channel depth w_v could be calculated as below:

$$w_v = l_{cuvette} \frac{\Upsilon(II)}{\Upsilon(I)} \quad \text{(S 3)}$$

where $l_{cuvette}$ was the thickness of the standard cuvette and equals to 10 mm, $\Upsilon(I)$ and $\Upsilon(II)$ were the slopes of the straight lines relating absorbance values to the molar concentrations of the dye ($\Upsilon = \frac{A}{c} = \varepsilon \cdot l$) in the systems (I) and (II), respectively. These slopes were fitted using the least squares method and are listed in Table S 2.

Table S 2 Calibration of the channel depth (w_v) in the cross-junction device: values of the fitted Υ deduced from Fig. S 4 for safranin and resorufin, in the cuvette and milli-channel systems.

System	Cuvette (I)	Milli-channel (II)	Cuvette (I)	Milli-channel (II)
Dyes	Safranin	Safranin	Resorufin	Resorufin
Υ (L mol^{-1})	32665	6962	19776	4219
	R^2=0.9972	R^2=0.9959	R^2=0.9993	R^2=0.9696

At last, the channel depths w_v were found at 2.1313 mm and 2.1334 mm with safranin and resorufin dyes respectively, leading to an average value equal to 2.13 mm (mean absolute deviation: 10^{-3}). This value is slightly higher than the designed 2 mm, which could be caused by the

sealing ring added between the top and middle plates and the bottom and middle plates.

The hydraulic diameter of the channel, noted d_h, is defined as below:

$$d_h = 2w_h w_v / (w_h + w_v) \quad \text{(S 4)}$$

The calculated hydraulic diameter d_h was then equal to 2.16 mm (mean absolute deviation: 0.03).

In addition, the molar attenuation coefficient ε could be further deduced through dividing the slope Υ by l, and were found at 3.3×10^4 and 2.0×10^4 L mol^{-1} cm^{-1} for safranin and resorufin dyes, which had the same order of magnitude than the values reported in the literature (for safranin 3.4×10^4 L mol^{-1} cm^{-1} (A Daher, 2012) and for resorufin 2.6×10^4 L mol^{-1} cm^{-1} (Siu et al., 2014) at 530nm). The relatively big differences of ε for RF may be caused by the presence of glucose and NaOH in the RF solution, and/or of impurities.

S2 Regions-of-interest (ROI) positions

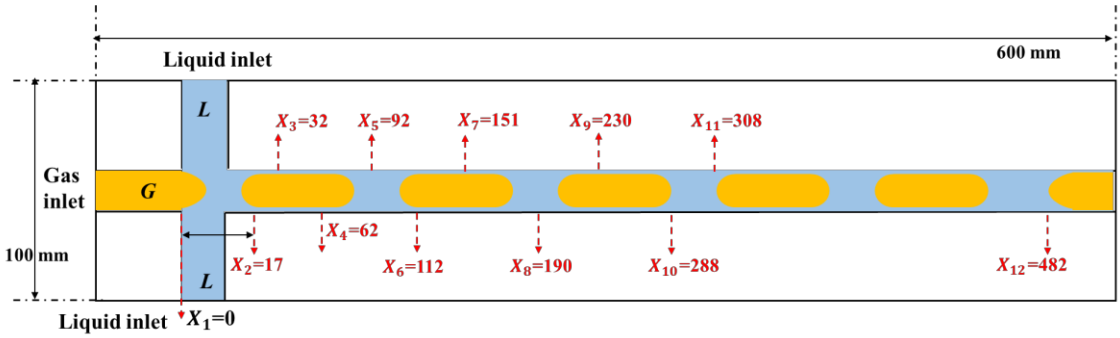

Fig. S 5 Geometry of the straight milli-channel with a cross-junction. The 12 axial positions, X (expressed in mm), corresponding to the various regions-of-interest (ROI), are marked by the red arrows. At $X = 0$, the two phases enter in contact.

S3 Bubble formation frequencies

Table S 3 Experimental data for the overall, filling and squeezing frequencies plotted in Fig.4.

j_L	j_{G0}	η_0	f_{filing}	$f_{squeezing}$	f_{BF}
cm s^{-1}	cm s^{-1}	(-)	Hz	Hz	Hz
7.2	3.6	0.5	62.75	9.42	8.19
7.2	7.2	1	66.67	11.25	9.63
7.2	14.3	2	81.63	16.10	13.45
7.2	21.4	3	100.00	18.18	15.38
14.3	7.2	0.5	50.63	33.97	20.33
14.3	14.3	1	67.80	50.09	28.81
14.3	21.4	1.5	95.24	45.09	30.60
17.9	10.7	0.6	58.82	67.68	31.47
17.9	17.9	1	80.00	71.26	37.69
17.9	25	1.4	72.73	96.83	41.53
17.9	35.7	2	93.02	92.30	46.33
21.4	7.2	0.3	48.78	95.01	32.23
21.4	14.3	0.7	60.61	112.90	39.44
21.4	21.4	1	71.43	127.25	45.75
21.4	32.2	1.5	90.91	148.19	56.34

S4 Bubble pinch-off pattern

Fig. S 6 Image processing for extracting the length of the gas finger right after the bubble pinch-off (j_L = 17.9 and j_{G0} = 25.0 cm s^{-1}): (a) raw image of gas finger, (b) extracted gas finger and l_{GF} represents the length of the gas finger.

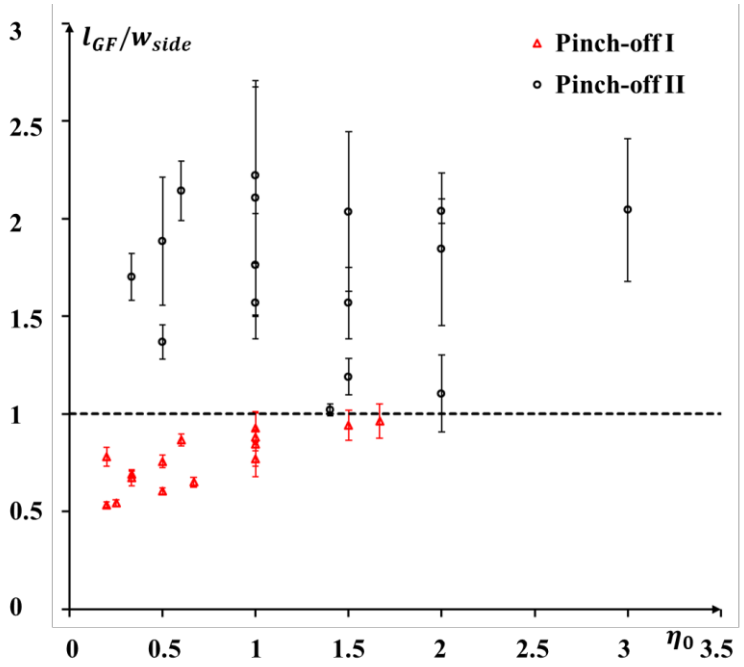

Fig. S 7 Identification of the bubble formation patterns obtained at the cross-junction: normalized gas finger length right after the bubble pinch-off versus the gas-liquid superficial velocity ratio.

It is noted that the standard deviations for the pinch-off pattern type II were significantly higher than those of pattern I. Due to the acquisition rate

(400 fps), one cannot exclude that the measured gas finger might not be equal to the gas finger right after the bubble pinch-off. To partly overcome this issue, for each operating condition, an average value was obtained using 1000 images, and then normalized by the width of the liquid inlet side channels (w_{side}, see Fig. S 6).

S5 Error analysis

The mean absolute percentage error of regression (MAPER) is expressed by the formula:

$$MAPER = \frac{1}{n}\sum_{i=1}^{n}\left|\frac{\varsigma_{actual} - \varsigma_{pre}}{\varsigma_{actual}}\right| \times 100\% \qquad \text{(S 5)}$$

S6 Bubble formation at the cross-junction in a straight milli-channel: experimental results of hydrodynamics characteristics

Table S 4 Experimental data on gas-liquid hydrodynamics in the straight milli-channel with a cross-junction

N.	j_L	j_{G0}	η_0	Re_L,	Re_G,	We_{TP}	Ca_{TP}, $\times 10^{-3}$	U_B	L_B / d_h	L_S / d_h	f_{BF}	ϖ
(-)	cm s^{-1}	cm s^{-1}	(-)	(-)	(-)	(-)	(-)	cm s^{-1}	(-)	(-)	Hz	(-)
1	7.2	21.4	3.0	140	31	2.4	4.3	29.2	6.37	1.39	15.38	1.0
2	11.4	17.2	1.5	221	25	2.4	4.3	29.2	3.69	1.54	22.64	0.9
3	14.3	14.3	1.0	278	21	2.4	4.3	29.2	2.79	1.69	28.81	0.8
4	17.9	10.7	0.6	347	16	2.4	4.3	29.2	2.07	1.99	31.47	0.8
5	21.4	7.2	0.3	415	11	2.4	4.3	29.2	1.6	2.59	32.23	0.6
6	14.3	21.4	1.5	278	31	3.7	5.3	36.4	3.69	1.54	30.60	0.9
7	17.9	17.9	1.0	347	26	3.7	5.3	36.4	2.79	1.69	37.69	0.8
8	21.4	14.3	0.7	415	21	3.7	5.3	36.4	2.19	1.92	39.44	0.8
9	28.6	7.2	0.3	555	11	3.7	5.3	36.4	1.45	3.04	38.08	0.7
10	17.9	25.0	1.4	347	37	5.3	6.4	43.7	3.51	1.56	41.53	0.8
11	21.4	21.4	1.0	415	31	5.3	6.4	43.7	2.79	1.69	45.75	0.8
12	28.6	14.3	0.5	555	21	5.3	6.4	43.7	1.9	2.14	49.28	0.7
13	35.7	7.2	0.2	693	11	5.3	6.4	43.7	1.36	3.49	45.00	0.5

Reference

A Daher, S., 2012. Determining values of some optical constants for some colorants. Journal of Education and Science 25, 79-86.

Cubaud, T., Ho, C.-M., 2004. Transport of bubbles in square microchannels. Physics of Fluids 16, 4575-4585.

De Gennes, P.-G., Brochard-Wyart, F., 2015. Gouttes, bulles, perles et ondes. Belin.

Doneux, T., Bouffier, L., Goudeau, B., Arbault, S.p., 2016. Coupling electrochemistry with fluorescence confocal microscopy to investigate electrochemical reactivity: a case study with the resazurin-resorufin fluorogenic couple. Analytical Chemistry 88, 6292-6300.

Fries, D.M., Trachsel, F., von Rohr, P.R., 2008. Segmented gas–liquid flow characterization in rectangular microchannels. International Journal of Multiphase Flow 34, 1108-1118. https://doi.org/10.1016/j.ijmultiphaseflow.2008.07.002

Mei, M., Hébrard, G., Dietrich, N., Loubière, K., 2020. Gas-liquid mass transfer around Taylor bubbles flowing in a long, in-plane, spiral-shaped milli-reactor. Chemical Engineering Science 222, 115717. https://doi.org/10.1016/j.ces.2020.115717

Ngai, J.H., Ho, J.K., Chan, R.K., Cheung, S., Leung, L.M., So, S., 2017. Growth, characterization, and thin film transistor application of CH 3 NH 3 PbI 3 perovskite on polymeric gate dielectric layers. Rsc Advances 7, 49353-49360.

Schulze, R.D., Possart, W., Kamusewitz, H., Bischof, C., 1989. Young's equilibrium contact angle on rough solid surfaces. Part I. An empirical determination. Journal of Adhesion Science and Technology 3, 39-48. https://doi.org/10.1163/156856189X00038

Siu, V.S., Feng, J., Flanigan, P.W., Palmore, G.T.R., Pacifici, D., 2014. A “plasmonic cuvette”: dye chemistry coupled to plasmonic interferometry for glucose sensing. Nanophotonics 3, 125-140.

Völkel, N., 2009. Design and characterization of gas-liquid microreactors.

Zrimšek, P., Kunc, J., Kosec, M., Mrkun, J., 2004. Spectrophotometric application of resazurin reduction assay to evaluate boar semen quality. International journal of andrology 27, 57-62.